The Astrophysical Journal Letters, 1000:L13 (29pp), 2026 March 20 https://doi.org/10.3847/2041-8213/ae48fd

exoALMA. XX. Tomographic Detection of Embedded Planets in Protoplanetary Disks

Andrés F. Izquierdo[1,2,28], Jaehan Bae[1], Stefano Facchini[3], Ewine F. van Dishoeck[2,4], Marcelo Barraza-Alfaro[5], Myriam Benisty[6], Richard Teague[5], Jochen Stadler[7,8], Sean M. Andrews[9], Gianni Cataldi[10], Nicolás Cuello[11], Pietro Curone[12], Ian Czekala[13], Daniele Fasano[7], Mario Flock[6], Misato Fukagawa[14], Maria Galloway-Sprietsma[1], Cassandra Hall[15,16,17], Jane Huang[18], John D. Ilee[19], Andrea Isella[20,21], Jensen Lawrence[5], Geoffroy Lesur[11], Giuseppe Lodato[3], Cristiano Longarini[22], Ryan A. Loomis[23], François Ménard[11], Christophe Pinte[11,24], Daniel J. Price[24], Giovanni Rosotti[3], Leonardo Testi[25], David J. Wilner[9], Andrew J. Winter[26], Lisa Wölfer[5], and Brianna Zawadzki[27]

[1] Department of Astronomy, University of Florida, Gainesville, FL 32611, USA; andres.izquierdo.c@gmail.com
[2] Leiden Observatory, Leiden University, P.O. Box 9513, NL-2300 RA Leiden, The Netherlands
[3] Dipartimento di Fisica, Università degli Studi di Milano, Via Celoria 16, 20133 Milano, Italy
[4] Max-Planck Institut für Extraterrestrische Physik (MPE), Gießenbachstr. 1, 85748, Garching bei München, Germany
[5] Department of Earth, Atmospheric, and Planetary Sciences, Massachusetts Institute of Technology, Cambridge, MA 02139, USA
[6] Max-Planck Institute for Astronomy (MPIA), Königstuhl 17, 69117 Heidelberg, Germany
[7] Université Côte d'Azur, Observatoire de la Côte d'Azur, CNRS, Laboratoire Lagrange, 06304 Nice, France
[8] European Southern Observatory, Karl-Schwarzschild-Str. 2, D-85748 Garching bei München, Germany
[9] Center for Astrophysics—Harvard & Smithsonian, Cambridge, MA 02138, USA
[10] National Astronomical Observatory of Japan, 2-21-1 Osawa, Mitaka, Tokyo 181-8588, Japan
[11] Université Grenoble Alpes, CNRS, IPAG, 38000 Grenoble, France
[12] Departamento de Astronomía, Universidad de Chile, Camino El Observatorio 1515, Las Condes, Santiago, Chile
[13] School of Physics & Astronomy, University of St. Andrews, North Haugh, St. Andrews KY16 9SS, UK
[14] National Astronomical Observatory of Japan, Osawa 2-21-1, Mitaka, Tokyo 181-8588, Japan
[15] Department of Physics and Astronomy, The University of Georgia, Athens, GA 30602, USA
[16] Center for Simulational Physics, The University of Georgia, Athens, GA 30602, USA
[17] Institute for Artificial Intelligence, The University of Georgia, Athens, GA, 30602, USA
[18] Department of Astronomy, Columbia University, 538 W. 120th Street, Pupin Hall, New York, NY, USA
[19] School of Physics and Astronomy, University of Leeds, Leeds, LS2 9JT, UK
[20] Department of Physics and Astronomy, Rice University, 6100 Main St, Houston, TX 77005, USA
[21] Rice Space Institute, Rice University, 6100 Main St, Houston, TX 77005, USA
[22] Institute of Astronomy, University of Cambridge, Madingley Road, CB3 0HA, Cambridge, UK
[23] National Radio Astronomy Observatory, 520 Edgemont Rd., Charlottesville, VA 22903, USA
[24] School of Physics and Astronomy, Monash University, Clayton VIC 3800, Australia
[25] Dipartimento di Fisica e Astronomia, Università di Bologna, I-40129 Bologna, Italy
[26] Astronomy Unit, School of Physics and Astronomy, Queen Mary University of London, London E1 4NS, UK
[27] Department of Astronomy, Van Vleck Observatory, Wesleyan University, 96 Foss Hill Dr., Middletown, CT, 06459, USA
Received 2025 December 15; revised 2026 February 6; accepted 2026 February 16; published 2026 March 16

Abstract

The exoALMA Large Program has revealed a wealth of substructures in the dust and molecular line emission of several protoplanetary discs, suggesting that planet formation may unfold within highly dynamic environments. Using synthetic observations of planet–disk interactions and disk instabilities, we demonstrate how the origin of these substructures can be investigated through a tomographic study of molecular lines, extending the scope of the analysis beyond line-centroid kinematics alone. Our results indicate that with only a few hours of ALMA integration at moderate angular resolution ($0\farcs15 - 0\farcs30$), it is possible to identify the key signatures driven by planets more massive than 0.1% of the stellar mass. These signatures manifest not only as deviations from Keplerian motion but also as localized line broadening, enabling accurate constraints on the orbital radius and azimuthal location of the planets. We further show that a diagnostic based on line skewness in spectrally resolved observations can help distinguish between planetary and instability-driven signatures, owing to the distinct degrees of velocity coherence associated with each mechanism. Finally, we apply this tomographic analysis to exoALMA CO line data for the disks of HD 135344B and MWC 758. In HD 135344B, we identify strongly localized velocity and line-width perturbations, suggesting the possibility of three massive planets embedded in the disk: one at $R = 95$ au, exterior to the continuum substructures, and two within dust gaps at $R = 41$ au and $R = 73$ au. For MWC 758, the dominance of vertical-velocity spirals over localized signatures is consistent with predictions from models of moderate disk eccentricities or warps, potentially induced by a substellar companion in the inner regions of the system.

Unified Astronomy Thesaurus concepts: Protoplanetary disks (1300); Planet formation (1241); Exoplanet detection methods (489); Planetary-disk interactions (2204)

1. Introduction

Sensitive and high-angular resolution Atacama Large Millimeter/submillimeter Array (ALMA) observations of protoplanetary disks are revolutionizing our understanding of the physicochemical mechanisms of planet formation. These

[28] NASA Hubble Fellowship Program Sagan Fellow.

data have revealed different families of dust and gas substructures in numerous disks (S. M. Andrews et al. 2018; K. I. Öberg et al. 2021; R. Teague et al. 2025; M. Fukagawa et al. 2026), potentially arising from the interplay between thermochemical processes (e.g., A. Miotello et al. 2023; K. I. Öberg et al. 2023) and physical mechanisms, including planet– and star–disk interactions (see C. Pinte et al. 2023, for a review), as well as gravitational and (magneto) hydrodynamical disk instabilities (e.g., J. Bae et al. 2023; G. Lesur et al. 2023).

In particular, the dynamical interaction between disks and planets is known to induce distinct signatures in molecular-line data, which can be broadly categorized into two groups according to their observed symmetry. The first group comprises axisymmetric substructures dominated by azimuthal velocity flows associated with pressure modulations around planet-carved gaps (e.g., R. Teague et al. 2018; G. P. Rosotti et al. 2020; A. F. Izquierdo et al. 2023; J. Stadler et al. 2025). The second group includes nonaxisymmetric patterns extending across the disk, typically in the form of spirals (e.g., R. Teague et al. 2021; J. Calcino et al. 2022; L. Wölfer et al. 2023), as well as localized kinematic perturbations (e.g., C. Pinte et al. 2018; S. Casassus & S. Pérez 2019; A. F. Izquierdo et al. 2022; J. Stadler et al. 2023) and chemical anomalies detected in the vicinity of embedded planets (C. J. Law et al. 2023; A. F. Izquierdo et al. 2026). A comparatively less explored feature in this group involves localized meridional flows induced by a planet, which lead to enhanced velocity dispersion. These flows arise from the interplay between planet-induced gravitational torques and viscous torques that act to refill the planet-driven gap from disk layers above the midplane (R. Dong et al. 2019; A. F. Izquierdo et al. 2023).

Similar observational features may, however, also arise from fluid instabilities that develop under specific disk conditions. For instance, nearly axisymmetric flows are a common outcome of the vertical shear instability (VSI; e.g., M. Barraza-Alfaro et al. 2021), which operates in thermally stratified disks with short cooling times that sustain differential rotation above the midplane. Spiral-like structures, by contrast, are more characteristic of gravitational instability (GI; e.g., C. Hall et al. 2020; J. Speedie et al. 2024), which occurs in sufficiently massive disks where self-gravity overcomes thermal and rotational support. Large-scale spiral morphologies, together with localized eddies, can also arise from the magnetorotational instability (MRI; e.g., M. Barraza-Alfaro et al. 2025), which develops in regions where the gas is sufficiently ionized for magnetic fields to couple to the flow and drive turbulence.

In this work, we quantify the detectability of planet-driven perturbations using exoALMA-like observations of three-dimensional planet–disk interaction simulations. We adopt a tomographic approach in which line broadening and line asymmetries are used as diagnostics of coherent velocity flows in the vicinity of embedded planets, and compare these signatures with those produced in VSI, MRI, and GI simulations. We then apply this analysis to two distinct exoALMA targets: the disk of HD 135344B, where multiple localized perturbations are identified, and MWC 758, where large-scale substructures predominate.

This Letter is organized as follows. Section 2 describes the observational data and channel-map models of the exoALMA targets analyzed in this study. Section 3 presents the extraction and characterization of observable features from models of planet–disk interactions and fluid instabilities. Section 4 illustrates the application of this methodology to the disks of HD 135344B and MWC 758. Section 5 discusses the interpretation of the detected signatures, and Section 6 highlights the main results of the work.

2. Data and Models

The ALMA data used in this Letter consist of exoALMA continuum-subtracted fiducial images of ^{12}CO and ^{13}CO $J = 3$ 2 for the disks of HD 135344B and MWC 758, as defined in R. Teague et al. (2025). These data cubes have a circular synthesized beam of $0\farcs15$ and a channel spacing of $0.1\,\mathrm{km\,s^{-1}}$. Details of the calibration and imaging procedures are provided in R. A. Loomis et al. (2025). We also use exoALMA fiducial continuum images centered at 0.9 mm from P. Curone et al. (2025), and Very Large Telescope (VLT)/SPHERE scattered-light images presented in T. Stolker et al. (2016) and M. Benisty et al. (2015). Channel-map models of the targets produced with DISCMINER, as reported by A. F. Izquierdo et al. (2025), are used as references to compute residual maps. These residuals enable the analysis of gas substructures that manifest as non-Keplerian motions and, more generally, as perturbations in the shape of the molecular-line profiles. The Keplerian stellar masses obtained from the channel-map models are 1.61 and 1.40 $M_\odot$ for HD 135344B and MWC 758, respectively, assuming Gaia-derived distances of 135 and 156 pc (Gaia Collaboration et al. 2023). The low disk inclinations of −16 and 19 , as inferred with DISCMINER, render the backside emission contribution negligible for both targets, resulting in line profiles that are generally symmetric about their centroids. We therefore characterize the line peaks, centroid velocities, and line widths of both the observed and modeled spectra by fitting single-Gaussian profiles along the spectral axis at each image pixel.

3. Analysis of Synthetic Observations

In this section, we present our analysis methodology for identifying gas substructures in molecular line images produced by planet–disk interactions and fluid instabilities, including VSI, MRI, and GI. The simulations are postprocessed to match the observational constraints of exoALMA, allowing us to assess the detectability of the associated signatures under realistic conditions. Residual maps of the analyzed mechanisms, obtained after subtracting smooth Keplerian DISCMINER models, are shown in Figure 1, with selected ^{12}CO intensity channels presented in Figure 18 of the Appendix.

3.1. Simulation Setup and Radiative Transfer

The planet–disk interaction simulations explored in this work were performed using the FARGO3D code (P. Benítez-Llambay & F. S. Masset 2016). This choice is not critical, however, as other hydrodynamic packages produce consistent observable kinematic signatures when analyzed through the same pipeline applied here (J. Bae et al. 2025). The simulations are set up following

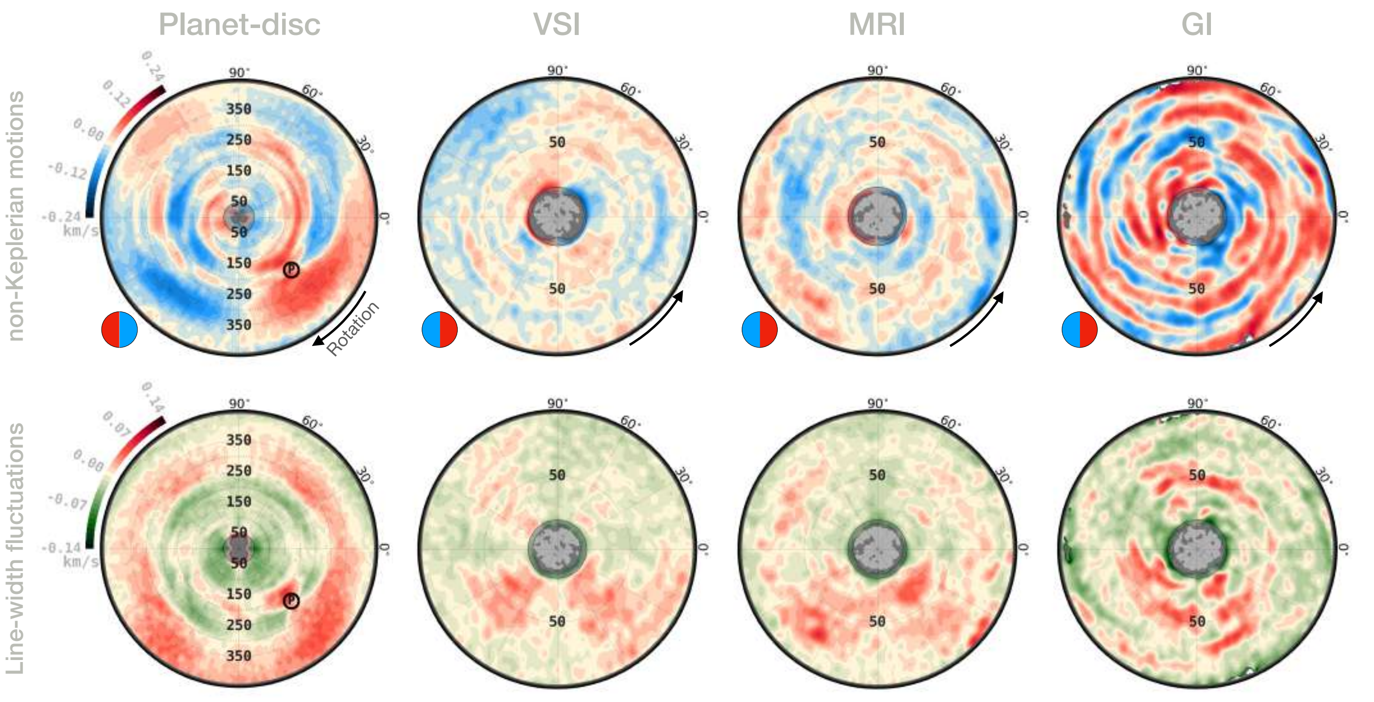

Figure 1. Velocity and line-width residuals derived from DISCMINER models applied to synthetic observations of planet–disk interaction ($q = 2 \times 10^{-3}$, $\phi_p = -45$) and disk instabilities. Details of the simulation setups are provided in Section 3.1. All disks are inclined by −30 , and the residuals from all mechanisms are shown on the same color scale indicated on the left. Semi-red/blue circles in the bottom left corners of the top-row panels indicate the locations of the redshifted and blueshifted sides of the simulated disk, which are useful to understand the velocity structure of the non-Keplerian flows (see Figure 2).

R. Teague et al. (2019), who aimed to reproduce the gas kinematics in the disk of HD 163296. In brief, the disk is initialized with a density distribution that satisfies the hydrostatic equilibrium and adopts a uniform alpha viscosity of $10.^{-3}$ The disk midplane and atmosphere follow independent power-law temperature distributions with radius, connected in the vertical direction by a squared-cosine function (E. Dartois et al. 2003). Instead of inserting multiple planets as in R. Teague et al. (2019), we run two single-planet simulations with planet masses of $M_p = 2\,M_{\rm Jup}$ and $4\,M_{\rm Jup}$ orbiting a $2\,M_\odot$ star, corresponding to planet-to-star mass ratios of $q \sim 1 \times 10^{-3}$ and $\sim 2 \times 10^{-3}$, respectively. The orbital radius of the planet is fixed at $R_p = 240$ au, while the azimuth ϕ_p is varied in eight increments of 45 to study the effects of projection and radiation transport on the retrieved perturbations along the entire disk circumference.

Radiative transfer calculations of CO line intensities were performed with RADMC3D (C. P. Dullemond et al. 2012), assuming a distance to the source of 101 pc and three disk inclinations: $i = -15$, -30 , and -45 . The central star is assumed to have a mass and luminosity of $2\,M_\odot$ and $17\,L_\odot$, respectively, similar to those of HD 163296 (J. R. Fairlamb et al. 2015). We assume that CO is fully photodissociated in surface layers of the disk where the vertically integrated gas density falls below 10^{21} cm^{-2} (R. Visser et al. 2009), and that CO is frozen onto dust grains in regions where the temperature drops below 21 K (K. R. Schwarz et al. 2016). For the remainder of the gas disk, we adopt a CO/H$_2$ abundance ratio of 10^{-5}.

Synthetic observations replicating the main properties of the fiducial images from exoALMA were generated using the SYNDISK code,[29] adopting a channel spacing of 0.1 km s^{-1}, and circular beams of 0″15 and 0″3. Two rms noise levels of 1.2 and 2.4 K were adopted for the fiducial 0″15 beam, corresponding to signal-to-noise ratios (SNRs) of ∼15 and ∼30 relative to the azimuthally averaged peak intensity of 35 K measured at the planet's orbital radius in the $q \sim 2 \times 10^{-3}$, $i = 15$ simulation. Under the same observational constraints, the larger 0″3 beam also used here yields an 8× increase in SNR.

The simulations and synthetic observations of the disk instabilities studied in this work are described in detail by M. Barraza-Alfaro et al. (2025). They were performed using the magnetohydrodynamics code PLUTO (A. Mignone et al. 2007) and were originally presented by M. Flock et al. (2020) for the VSI, M. Flock et al. (2015) for the MRI, and W. Béthune & H. Latter (2022) for GI. In all cases, the adopted stellar mass was $M_\star = 0.5\,M_\odot$, with a self-gravitating disk mass of $0.1\,M_\odot$ in the GI simulation, and a disk inclination of $i = -30$. For the postprocessing stage, we generate synthetic ^{12}CO $J = 3$ 2 emission for each mechanism using RADMC3D, assuming a source distance of 140 pc, a channel spacing of 0.1 km s^{-1}, and a ^{12}CO abundance of 10^{-4}, reduced by a factor of 10^5 in regions of the disk where the temperature falls below 21 K (to emulate CO freeze-out) or where the vertically integrated gas column density drops below 10^{21} cm^{-2} (to account for CO photodissociation). Since the physical domains of the simulations are typically smaller (∼100 au) than those of most exoALMA disks, the angular resolution of the synthetic observations was set to 0″035 in order to sample the disk radial extent with ∼20 resolution elements, consistent with the average of our targets. The rms noise level was set to 1.3 K, yielding SNRs between 15 and 30 relative to the measured peak intensities across the disk.

[29] https://github.com/richteague/syndisk

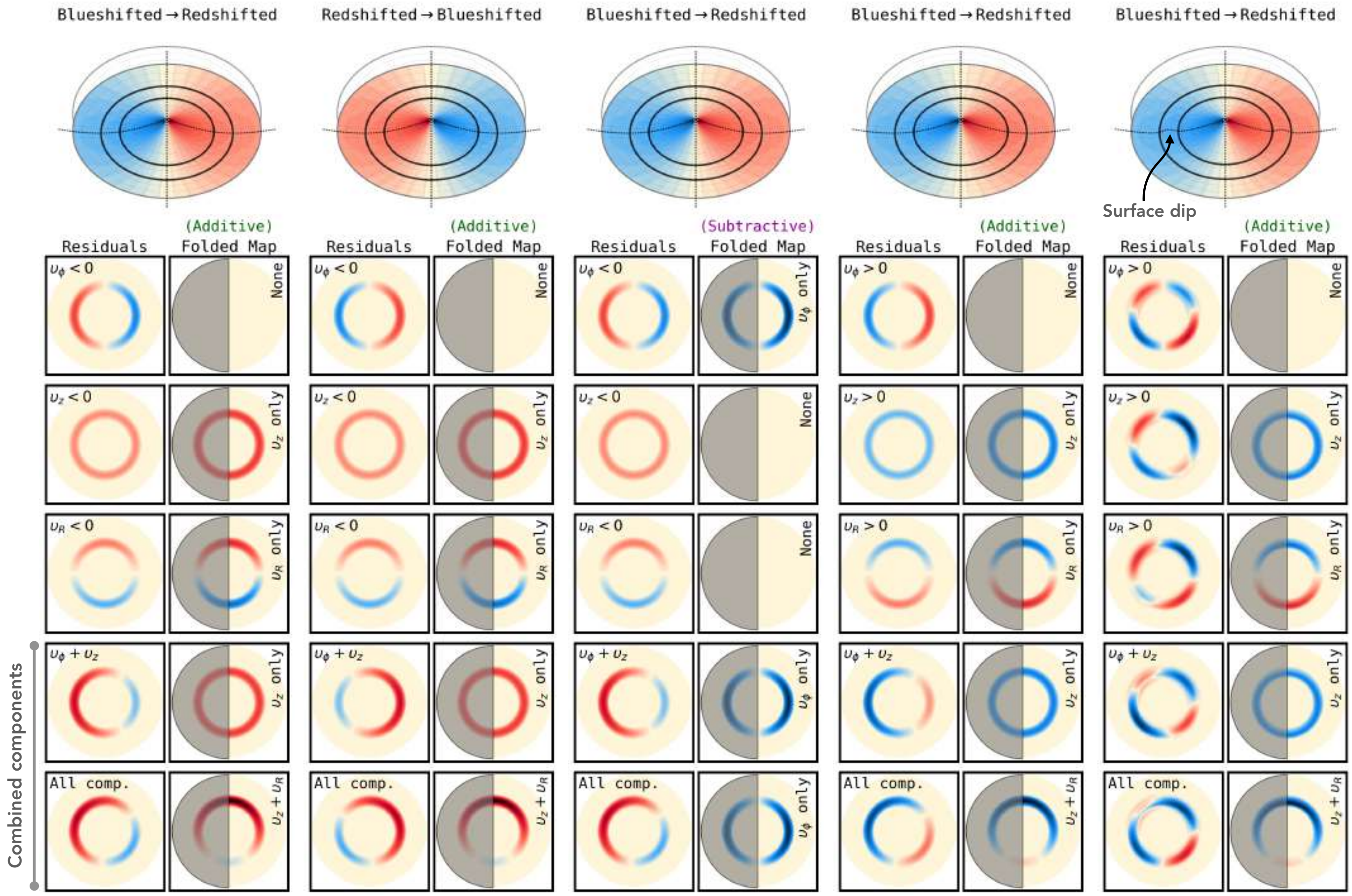

Figure 2. Illustrating axisymmetric velocity residuals for different combinations of velocity components, projected disk rotation, and the resulting folded maps obtained using either the additive or subtractive folding method. The first three columns show residuals for negative velocity flows after subtraction of a Keplerian model, while the following two focus on positive ones. In this context, *positive* denotes super-Keplerian motion for v_ϕ, outward motion in cylindrical radius for v_R, and upward motion relative to the disk midplane for v_z. The rightmost column shows a scenario where the underlying disk emission surface includes a dip (30 au wide and 20 au deep) that is not considered by the subtracted model. This substructure introduces an antisymmetric contribution to the residuals around the disk minor axis, which is consequently filtered out after additive folding.

3.2. Folded Maps and Localized Signatures

Embedded planets are known to induce localized perturbations in the dynamical and physical structure of their host disks (e.g., S. Pérez et al. 2018; R. Dong et al. 2019). To identify such signatures in our simulated data, we search for high-amplitude, spatially clustered residuals in folded velocity and line-width maps following the approach of A. F. Izquierdo et al. (2021). By applying this folding procedure, which compares two-dimensional maps of these line-profile properties on the redshifted and blueshifted sides of the disk, we can selectively isolate nonaxisymmetric perturbations driven by planets and other mechanisms.

Folded maps – For velocities, folded maps can be constructed either by adding or subtracting one side of the disk from the other, depending on which velocity components are to be suppressed. As illustrated in Figure 2, additive folding minimizes the contribution of axisymmetric azimuthal velocity flows (e.g., those prominent around gas gaps, A. F. Izquierdo et al. 2023; M. Benisty et al. 2026), whereas subtractive folding is more effective at filtering out axisymmetric vertical or radial velocity components (e.g., J. Stadler et al. 2023). Since azimuthal velocity flows typically dominate around surface-density gaps (J. Stadler et al. 2025) and on global scales primarily due to the disk Keplerian rotation (C. Longarini et al. 2025), we adopt additive folding as the default method for reducing velocity maps unless otherwise specified. Conversely, because line width is a scalar quantity, we search for localized enhancements in this property using subtractive folding. Peak intensities are excluded from this analysis, as for the optically thick line adopted, they respond more strongly to large-scale temperature fluctuations than to the local influence of the planet. However, they may still be valuable for optically thinner tracers that probe closer to the midplane, where they can capture both temperature and density anomalies in the planet's vicinity.

Localized signatures – We take the locations of global peak residuals as proxies for embedded planets. These are derived from a two-dimensional distribution of peak velocity and line-width values extracted per annulus from the folded maps, with annuli spaced at intervals of one-fifth of the beam size. A global peak is considered significant when it exceeds 3σ relative to the mean value of all identified peaks, where σ denotes the standard deviation of the peak distribution. As a less conservative alternative, and to avoid bias from the candidate itself inflating the noise value, we additionally evaluate a scatter estimator of the peak distribution (p) based on the median absolute deviation (MAD), defined as

$$\sigma_{\rm MAD} = 1.4826 \times \text{median}(|p - \text{median}(p)|), \quad (1)$$

which provides a Gaussian-equivalent estimate of the standard deviation for normally distributed data while remaining insensitive to a small number of outliers (e.g., C. Leys et al. 2013), such as planet-induced peaks. Hence, $\sigma_{\rm MAD}$ offers a more representative measure of the background disk perturbations away from the planet vicinity.

We also apply a K-means algorithm to identify localized clusters of residuals across both the azimuthal and radial extents of the disk as additional indicators of planet locations. The clustering analysis uses the same distribution of peak velocity and line-width residuals extracted from the folded maps. A cluster is classified as significantly localized and coherent when its variance exceeds the mean variance of all other clusters identified in the disk by more than 3σ, where σ denotes the standard deviation of the cluster-to-cluster variance distribution.

3.2.1. Planet-driven Signatures

Figure 3 illustrates a subset of the folded maps obtained from our planet–disk interaction models, highlighting the localized line-width and velocity signatures induced by the embedded planet. These maps correspond to models with a planet-to-star mass ratio of $q \sim 2 \times 10^{-3}$ and are extracted from images convolved to beam sizes of 0.″15 (with SNR $\sim$ 30) and 0.″3, assuming a disk inclination of $i = -30$.

Line width vs. velocity signals – For the 0.″15 beam, detections based on line-width residuals are successful for all eight planet azimuths considered, with median offsets of 6.2 au in radius (i.e., less than half a beamwidth) and 6.°0 in azimuth relative to the true planet position. The corresponding median detection significances across planet azimuths are 4.3σ with respect to all peak residuals and 8.3σ when referenced to the scatter estimate $\sigma_{\rm MAD}$ (Equation (1)), which is less sensitive to the strong outliers associated with the planet signal. Under the same setup, these metrics are considerably improved for an inclination of $i = -15$, yielding median offsets of 0.9 au in radius and 1.°5 in azimuth, and median detection significances of 5.3σ relative to all peaks and 15.5σ with the MAD estimator. For $i = -30$, the line-width signals are detected as highly clustered in six of the eight planet azimuths; planets at $\phi_p = -135$ and $\phi_p = -90$ are identified only through global peak values. For $i = -15$, planets at all azimuths are detected using both global peak and clustered residuals.

Detections based on velocity residuals are significantly less robust, with success rates of $2/8$ and $4/8$ for inclinations of $i = -30$ and $i = -15$, respectively. They also yield considerably lower significances than those based on line widths. For the detected signals at $i = -30$, we obtain a median significance of 3.1σ relative to all peaks and 6.1σ using the MAD estimator, while at $i = -15$ the corresponding values are 3.1σ and 4.3σ. The similarity between the all-peak and MAD significances indicates that the peak velocity residuals are more nearly normally distributed than the line-width residuals, implying a weaker dominance of the planet-driven signal with respect to background disk fluctuations.

This behavior arises because strong velocity perturbations develop not only in the immediate vicinity of the planet but also at larger radial and azimuthal separations, particularly for high-mass planets or in the presence of fluid instabilities. A similar result was reported by A. F. Izquierdo et al. (2021), who showed that the signals induced by their most massive planet ($3\,M_{\rm Jup}$, or $q \sim 3 \times 10^{-3}$) were less localized in velocity than those produced by lower-mass planets. Crucially, we note that this effect is likely further exacerbated by the large-scale vertical motions driven by the planet, which were not included in the two-dimensional simulations of A. F. Izquierdo et al. (2021). Additionally, as illustrated in Figure 19 in the Appendix, this effect can be amplified by projection; depending on the planet's azimuthal location, multiple velocity components may add coherently (or destructively) along the line of sight at regions far from (or near) the planet, thereby competing with the localized signal associated with the embedded object.

Despite these challenges, velocity residuals remain a valuable diagnostic of planet presence. As shown in Figure 20 of the Appendix, although the velocity perturbations around the modeled planet are not strongly localized relative to background fluctuations, they still respond to the large-scale pressure modulation associated with the carved gap, and produce pronounced azimuthal gradients linked to the planet-induced Doppler flip, defined as a local reversal in the sign of the velocity signal across the planet location (e.g., S. Pérez et al. 2018; I. Rabago & Z. Zhu 2021; A. F. Izquierdo et al. 2022).

Line-width signal vs. planet azimuth and beam size – By contrast with velocity residuals, the amplitude of the detected line-width signals shows a minimal dependence on the planet's azimuth, as demonstrated in Figure 4, making it a more direct proxy for planet mass. An additional advantage of this diagnostic is its robustness to beam size; although degrading the angular resolution reduces the observed amplitude of the perturbations, their detectability remains largely unaffected. For a planet-to-star mass ratio of $q \sim 2 \times 10^{-3}$, we estimate a decrease in the median peak line width across planet azimuths from 124 m s^{-1} at a beam size of 0."15 to 74 m s^{-1} at 0."3. However, in all cases, the coarser beam does not compromise the accuracy of the recovered planet location, highlighting the feasibility of systematically searching for planets even in lower-resolution data or in images deliberately degraded to improve the SNR.

Planet mass detection limit – The line-width peaks from the $q \sim 1 \times 10^{-3}$ hydro models are typically identified near the true planet azimuths but lie close to the 3σ threshold relative to both the all-peak and background (MAD) fluctuations. This suggests that a planet with a mass comparable to Jupiter orbiting a solar-mass star provides a reasonable lower bound for the detection of planet-driven line broadening at the adopted orbital radius and under the observational constraints of exoALMA. This estimate is consistent with the lowest-mass planet independently inferred by C. Pinte et al. (2025) to reproduce kink-like features in channel maps of the exoALMA targets.

Detection robustness across parameter space – We extend this analysis by summarizing the robustness of line-width peak detections across all adopted disk inclinations, SNRs, planet masses, azimuths, and beam resolutions in Figure 5. This is quantified using a scoring system ranging from 0 to 1, where a score of 1 corresponds to a detection located exactly at the planet's true position with a significance of at least 3σ. The score is defined as the product of three unit-amplitude Gaussian functions that evaluate the detection's proximity to the planet in radial and azimuthal coordinates, as well as its significance. The two spatial Gaussians adopt standard

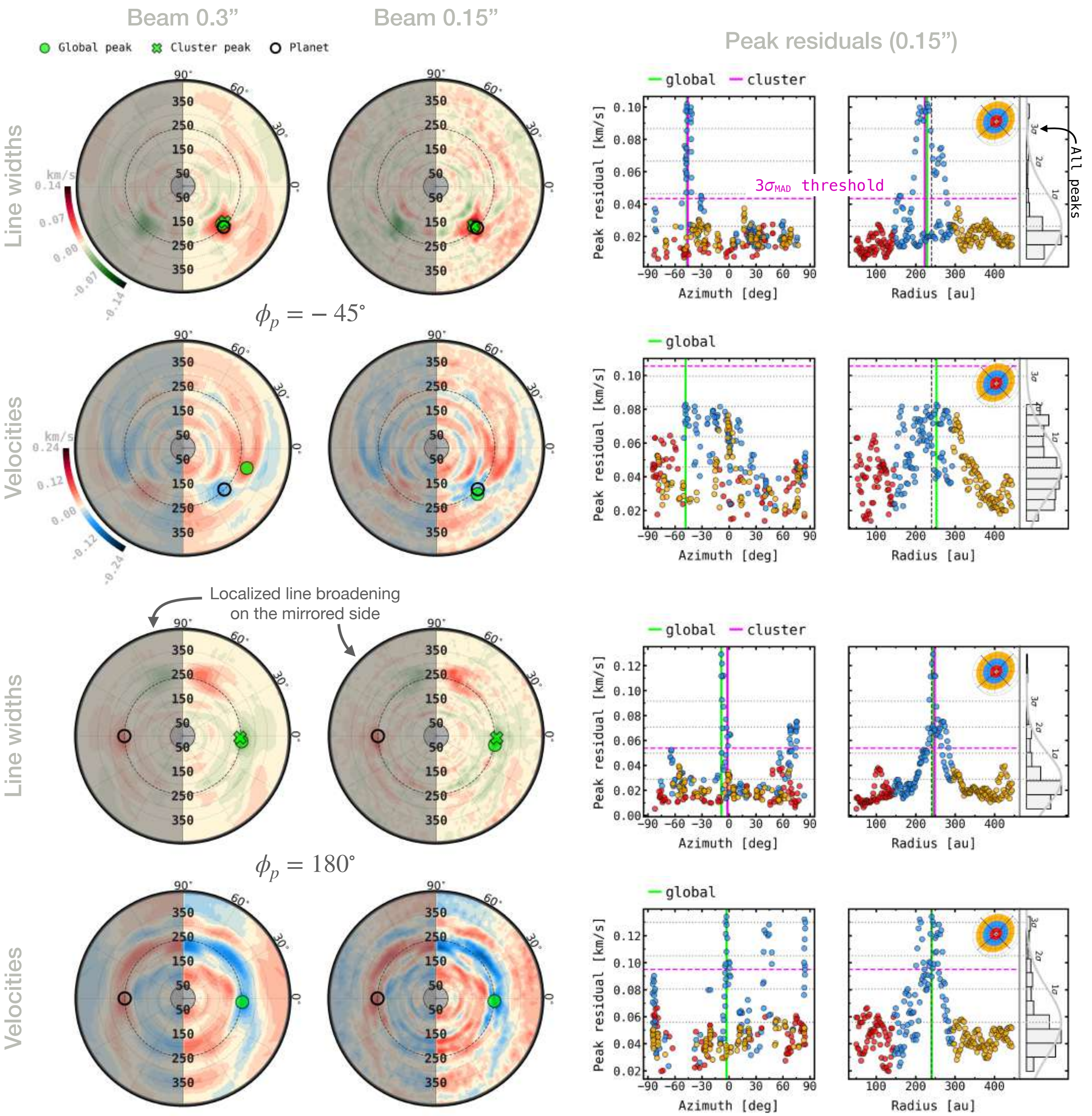

Figure 3. Illustration of the localized signatures identified in folded line-width and velocity residuals traced by ^{12}CO emission from a planet–disk interaction simulation with a planet-to-star mass ratio of $q \sim 2 \times 10^{-3}$, assuming a disk inclination of $i = -30$. Results are shown for two planet azimuths, $\phi_p = -45$ and 180 , and for two beam sizes, 0″3 and 0″15. Green circles and crosses mark the locations of peaks and clustered residuals, while the unfilled circle denotes the true planet position. A signal is considered detected when its global peak exceeds a significance of 3σ, as indicated by the horizontal dotted and dashed lines, corresponding to thresholds defined using all peak residuals and the MAD estimator, respectively. Detections based on line widths have a higher success rate due to their stronger spatial localization (clustered residuals), compared to their velocity counterparts, which in this example remain undetected for the $\phi_p = -45$ planet and only marginally detected for $\phi_p = 180$. Since embedded planets are expected to produce localized line-width enhancements rather than reductions, the sign of the line-width signal also helps resolve the ambiguity between opposite sides of the disk introduced by the folding process.

deviations of $\sigma_r = 35$ au, corresponding to half the radial width of the pressure modulation induced by the planet (or 1–2 beams), and $\sigma_\phi = 20$, equivalent to an azimuthal slice of $1/18$th of the disk circumference. The significance Gaussian is capped at 3σ and decreases normally for lower values, making the metric only weakly dependent on the choice of scatter estimator (σ or σ_{MAD}) introduced in Section 3.2. Under these definitions, any planet with a score above 0.6 (blue squares) satisfies the condition of being detected within its radial pressure bump and azimuthal sector, with a significance of at least 3σ. The same analysis is performed using peak velocity residuals, as illustrated in Figure 21 of the Appendix.

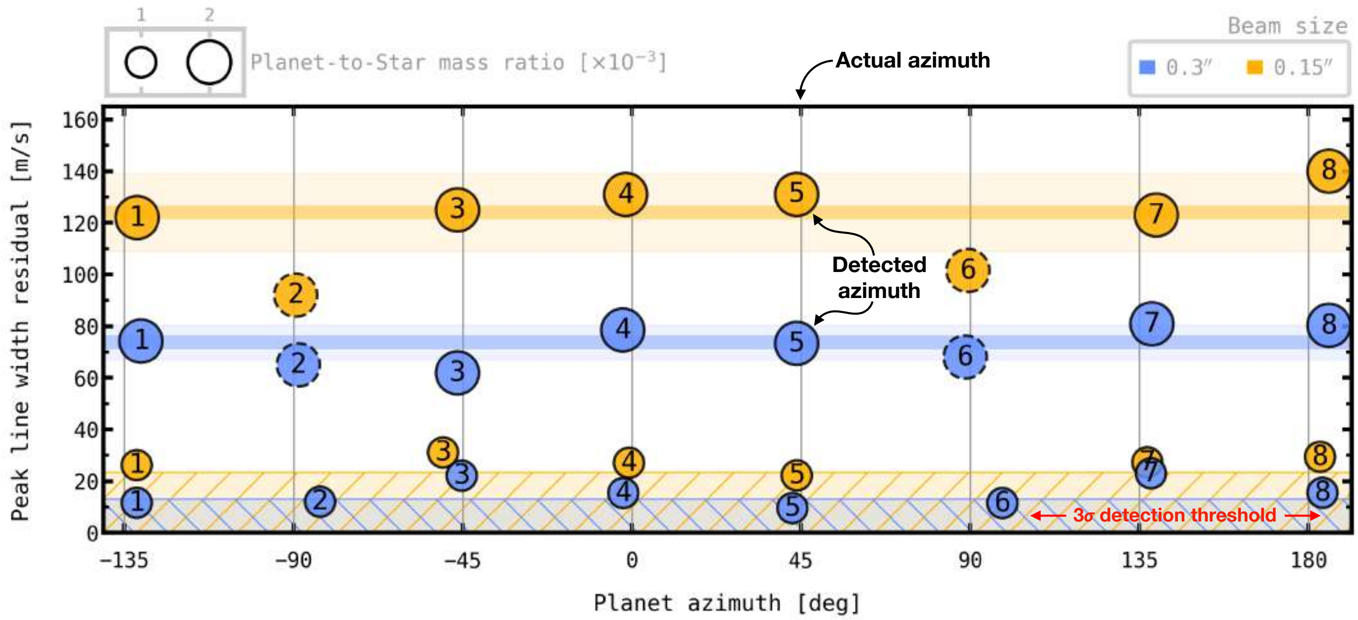

Figure 4. Detected amplitude of folded line-width perturbations as a function of the inferred planet azimuth in synthetic observations of the planet–disk interaction simulations introduced in Section 3.1, for different planet masses and beam sizes, and a disk inclination of $i = -15$. Although increasing the beam size from 0$''$.15 to 0$''$.3 weakens the observed signal around the planet, its detectability is not compromised, suggesting that relatively inexpensive ALMA observations are sufficient to robustly detect planets with 0.2% the mass of the star and marginally detect those with 0.1%. Line-width amplitudes shown as filled circles were measured using subtractive folding of the disk, whereas dotted circles, corresponding to planets located along the disk minor axis, were obtained using additive folding (followed by division by two) to avoid self-subtraction of the signal in the former method. Vertical lines indicate the true planet azimuths used in each of the eight simulation snapshots. Horizontal lines and shaded regions denote the median and standard deviation of the peak values, respectively, while hatched areas mark the median 3σ detection threshold for the low-mass planet simulations.

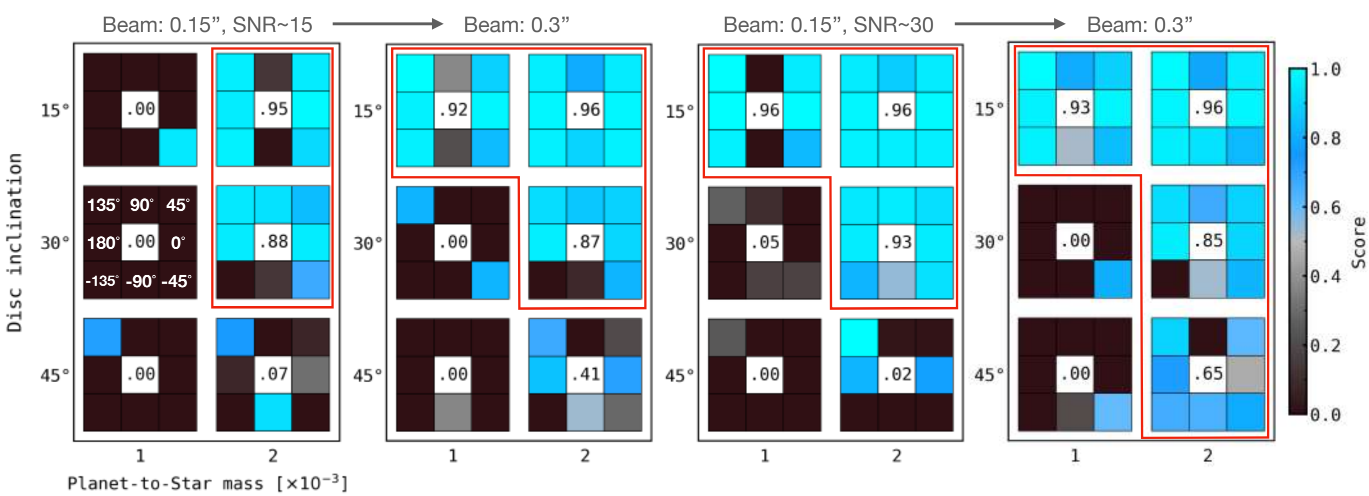

Figure 5. Goodness of planet detections based on localized line widths across all disk inclinations, planet masses and azimuths, beam sizes, and SNRs. Subsquares represent the eight adopted planet azimuths (from −135 to 180 in steps of 45). A score of 1 corresponds to a planet detected at its true location with a significance of at least 3σ. The score is defined as the product of three Gaussian functions evaluating the proximity of the detection in radial and azimuthal coordinates, as well as its significance. Planets with scores above 0.6 (blue subsquares) are detected within their radial pressure bump and azimuthal sector, with a significance of at least 3σ. Central subsquares indicate the median score across all planet azimuths, with those exceeding 0.6 outlined in red to highlight the inclination-mass configurations where planet-driven line broadening is detectable for each adopted beam size and SNR.

Effect of SNR, beam size, and channel spacing – Regardless of the SNR or angular resolution employed, line-width features are robustly detected for disk inclinations of −15 and −30 for the highest planet mass considered ($q \sim 2 \times 10^{-3}$). Importantly, doubling the SNR at fixed beam size substantially enhances the detectability of these signatures for the lower-mass planet ($q \sim 1 \times 10^{-3}$) and for the higher inclination of −45 . This analysis further indicates that lower angular resolution does not necessarily hinder detectability; in some cases, it reveals features that remain undetected in higher-resolution (but lower-SNR) images and can even enhance the significance of the planet signal at larger disk inclinations.

Similarly, adopting coarser channel spacings by factors of 2–3 does not compromise the detectability of either line-width or velocity signals, as illustrated in Figures 6 and 7. However, in contrast to degrading angular resolution, the amplitudes of the planet signals remain largely unaffected until channelization effects begin to dominate. This suggests that relaxing the

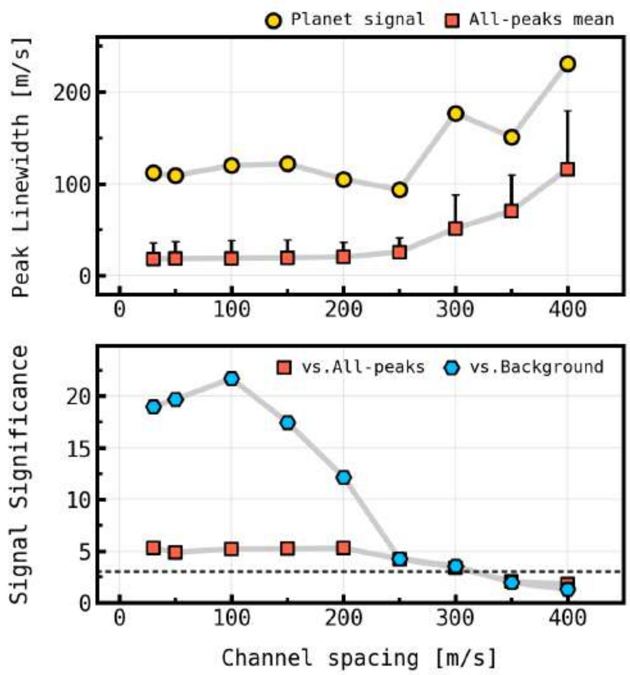

Figure 6. Peak line-width residual as a function of the channel spacing for the planet–disk interaction model with a planet-to-star mass ratio of $q = 2 \times 10^{-3}$, an inclination of $i = -15$, and a planet azimuth of $\phi_p = -45$, imaged with a beam size of 0$''$15 and an SNR of $\sim$30 (at $\Delta v = 0.1$ km s^{-1}). Also shown is the detection significance of the signal relative to the full distribution of peak residuals and to the MAD of the background, which is considerably less affected by planet-driven outliers.

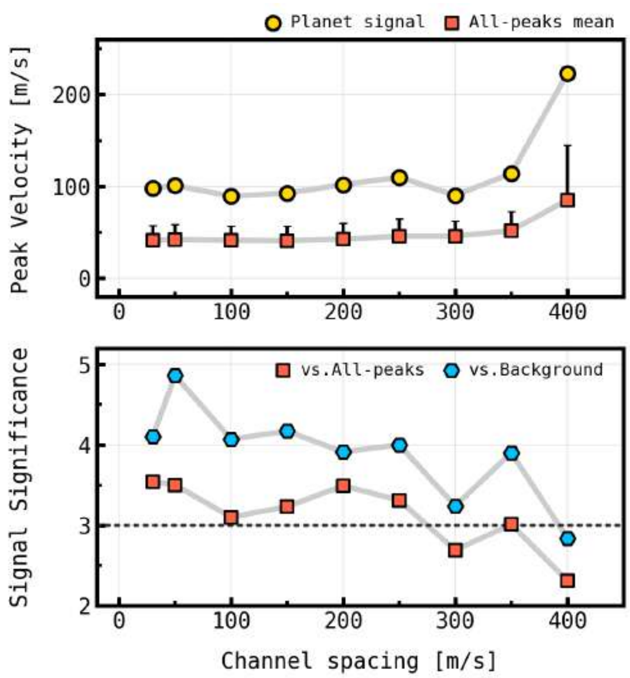

Figure 7. As Figure 6, but for peak velocity residuals.

spectral resolution may be a viable observational alternative for boosting SNR without sacrificing planet detectability or angular resolution, particularly when probing the innermost regions of the disk where beam smearing can significantly suppress perturbations in the planet's vicinity.

3.2.2. Localized Signatures of Disk Instabilities

Although the kinematic structures produced by disk instabilities are predominantly characterized by large-scale residuals, consistent with previous studies (e.g., C. Hall et al. 2020 for GI; M. Barraza-Alfaro et al. 2021 for VSI), localized perturbations can also arise in observations of these mechanisms. This is illustrated in Figure 8, which presents folded velocity and line-width residuals together with the locations of global peaks and clusters above the 3σ detection threshold. Among the localized signals identified, the highest significance (in the MRI line-width maps) reaches only 3.5σ, lower than the typical values (>4σ) obtained for the planet–disk simulation with $q \sim 2 \times 10^{-3}$, though comparable when the planet mass is reduced by half. Nevertheless, we do not identify complementary signatures that could plausibly mimic a planetary origin, as summarized in Figure 20 of the Appendix. For instance, variations in the rotation velocity associated with pressure modulations, or local minima in azimuthally averaged line widths indicative of a gap, are absent at the locations of the detected features.

Crucially, we find that the morphology of the line broadening associated with the signals detected in the disk-instability models is substantially more symmetric about the line centroid than in the case of an embedded planet, indicating an intrinsic difference in the projected motions responsible for the observed line-width enhancements. As discussed in the next section, this behavior provides a robust diagnostic for distinguishing localized planet-driven signatures from substructures induced by disk instabilities.

3.3. Line Asymmetries and Intensity Distributions: Planets versus Disk Instabilities

To investigate the origin of the localized features in the planet–disk and disk-instability simulations, we examine the observed intensity distributions and stacked line morphologies around the detected signals in Figure 9. The most prominent difference is that the planet-driven line broadening arises from intensity distributions that are significantly more skewed toward low intensities and blueshifted velocities than those found in quiescent regions of the disk. This pattern is consistently observed around the line-width features detected across all other planet–disk simulations, regardless of the planet azimuth, beam size, or SNR. In contrast, regions of enhanced line width in disk instabilities exhibit intensity distributions centered at higher intensity values relative to other areas of the disk and show no significant asymmetries in velocity.

The pronounced line asymmetries induced by the planet in its vicinity point to intricate yet structured motions probed by the observations. They indicate that coherent velocity flows capable of producing multicomponent spectra dominate in the planetary case, whereas more isotropic motions prevail in the disk instabilities. For reference, in planet–disk synthetic observations with a beam size of 0$''$3 and a disk inclination of $i = -15$, we measure a blue-to-redshifted line asymmetry[30] of 103   3 m s^{-1} for a planet with 0.2% the mass of the star, and 50   3 m s^{-1} for a planet of 0.1%.

[30] Defined as the difference between the velocities at the 16th (blueshifted) and 84th (redshifted) percentiles of the line profile, computed with BETTERMOMENTS, after subtraction of the same quantity measured from the reference DISCMINER model.

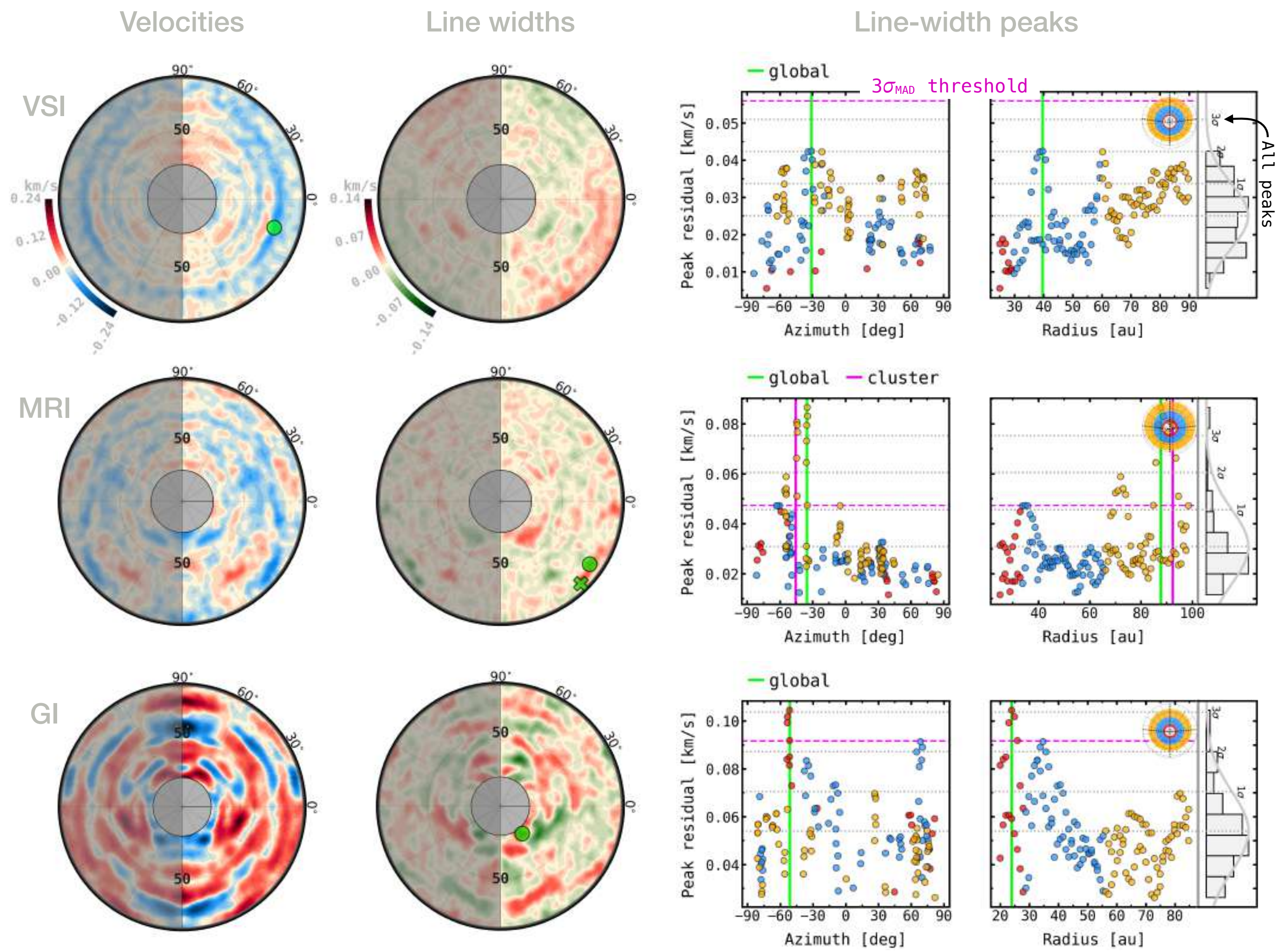

Figure 8. Folded velocity and line-width maps for the disk-instability simulations, showing the detected global peaks (green circles) and clusters (crosses) above the 3σ threshold. The right-hand panels display the distribution of peak line-width residuals as a function of the azimuth and radius, which are used for signal extraction and are color coded according to the radial region of the disk from which they were derived. In Section 3.3, we examine the spectral origin of these signals in comparison with the planet–disk interaction scenario.

We attribute these asymmetries to meridional flows converging toward the planet, consistent with the velocity structure predicted by the simulations (see Figure 22 in the Appendix). These flows are traced in the warm upper layers on the front side of the disk, where they predominantly recede relative to the observer and therefore produce a bright redshifted component in the ^{12}CO line profile. In contrast, the mirrored velocity counterpart on the opposite side of the midplane (i.e., the backside) is largely suppressed by the high optical depth of the line, resulting in a deficit of blueshifted intensity. If the disk is thermally stratified, as observations systematically suggest (M. Galloway-Sprietsma et al. 2025), this asymmetry is expected to be even more pronounced, since only gas from the colder lower layers on the backside (at velocities sampling the optically thinner line wings) can contribute to the observed blueshifted emission.

To demonstrate this behavior, we ran simulations using the optically thinner tracer ^{13}CO $J = 3$ 2 and extracted line profiles at the same locations for all mechanisms (see Figure 23 in the Appendix). In the planet–disk interaction model, localized line broadening is still detected at the planet location, but the line-intensity asymmetries vanish, confirming that, in this case, converging motions from above and below the midplane contribute more equally to the observed emission. For the disk instabilities, the ^{13}CO lines remain similarly symmetric about their centroids as in the ^{12}CO models, indicating that the velocity fluctuations responsible for the line-width enhancements in these mechanisms are also vertically isotropic.

Another consequence of the velocity asymmetries induced by planets in optically thick observations is an increase in the uncertainty of the line-centroid measurements in the planet's vicinity. As illustrated in Figure 10, this effect also produces a highly localized and clustered signal at the planet's location, whereas for the disk-instability models, the corresponding uncertainties are distributed more broadly across the disk and show no significant correlation with the velocity or line-width substructures identified in the residual maps.

4. Application to the Disks of HD 135344B and MWC 758

The disks of HD 135344B and MWC 758 are characterized by the presence of gaps, rings, arcs, and spiral patterns in continuum emission, potentially induced by massive yet unseen embedded planets (e.g., A. Garufi et al. 2013; R. Dong et al. 2015). Here, we apply our tomographic analysis of

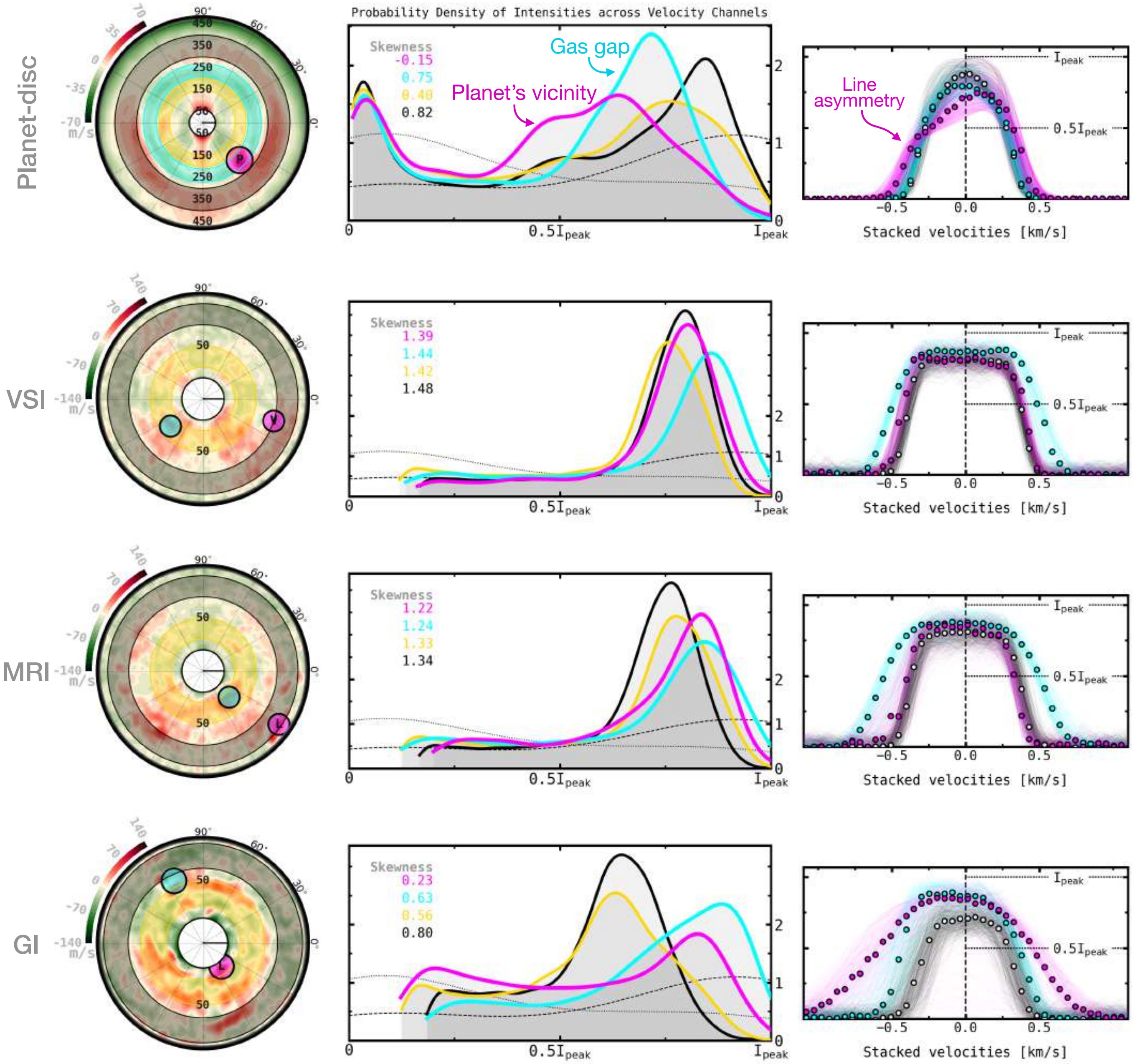

Figure 9. Comparison of ^{12}CO intensity distributions and line-profile morphologies for the mechanisms explored in this work. The left column shows line-width residuals overlaid with the regions analyzed. The middle column presents the probability density functions of intensities from the regions highlighted on the left with the same color code, computed across all velocity channels. For reference, the dotted and dashed lines show the probability densities obtained for a Gaussian and a thick-Gaussian profile, respectively, assuming the same rms level and channel spacing of the synthetic data. In the planet–disk scenario, the magenta curve corresponds to the intensity distribution in the planet's vicinity ("*P*" on the left), while the blue curve traces the gap region. For the disk instabilities, the magenta curves indicate regions of enhanced line widths or velocities ("*L*" or "*V*" on the left) detected above the 3σ threshold (in Figure 8), while the blue curves represent other selected areas with increased line width for comparison. In all cases, the yellow and black curves represent the innermost and outermost parts of the disk. The reported skewness values are computed directly from the probability densities, with low and high values corresponding to flatter and more peaked distributions, respectively. The right column shows 500 randomly drawn spectra from each region, stacked in velocity after deprojection assuming Keplerian rotation. These comparisons highlight that the line broadening associated with disk instabilities is relatively isotropic, whereas planet–disk interactions produce extended tails toward low intensities and velocities, responding to the presence of high velocity gradients and coherent flows around the planet.

molecular-line data to investigate the possible planetary origin of the gas and dust structures identified in these systems.

Figure 11 presents a gallery of the residual maps derived for these sources, obtained by subtracting the best-fit DISCMINER models of the ^{12}CO $J = 3 - 2$ line emission following A. F. Izquierdo et al. (2025). Both disks exhibit a high degree of substructure across all residual diagnostics: peak intensity, which closely traces temperature variations due to the high optical depth of the tracer; line width, which responds to surface-density and temperature fluctuations as well as unresolved velocity flows; and velocity centroids, which probe deviations from Keplerian rotation.

Localized features are particularly prominent in the velocity map of HD 135344B, manifested as sharp sign reversals (or

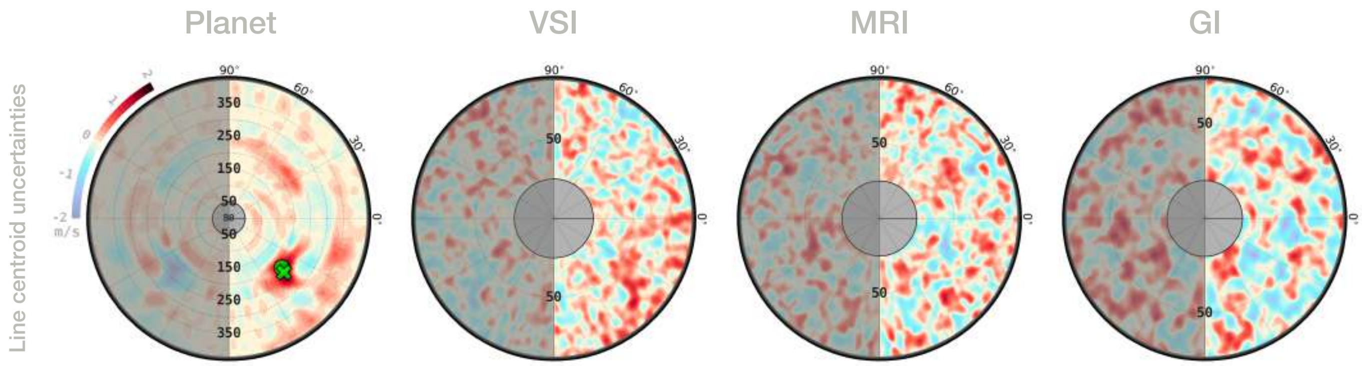

Figure 10. Folded maps of line-centroid uncertainties extracted from the Gaussian least-squares fits to the line profiles of the planet–disk and disk-instability simulations. This quantity is computed as the square root of the absolute value of the diagonal elements of the covariance matrix returned by the fit. A localized and coherent signal is detected only around the planet's location in this observable, resulting from the strong line asymmetries induced by the embedded planet in its vicinity, as demonstrated in Figure 9 (top right). No strong correlation is found between these residuals and the velocity or line-width substructures observed in disk instabilities.

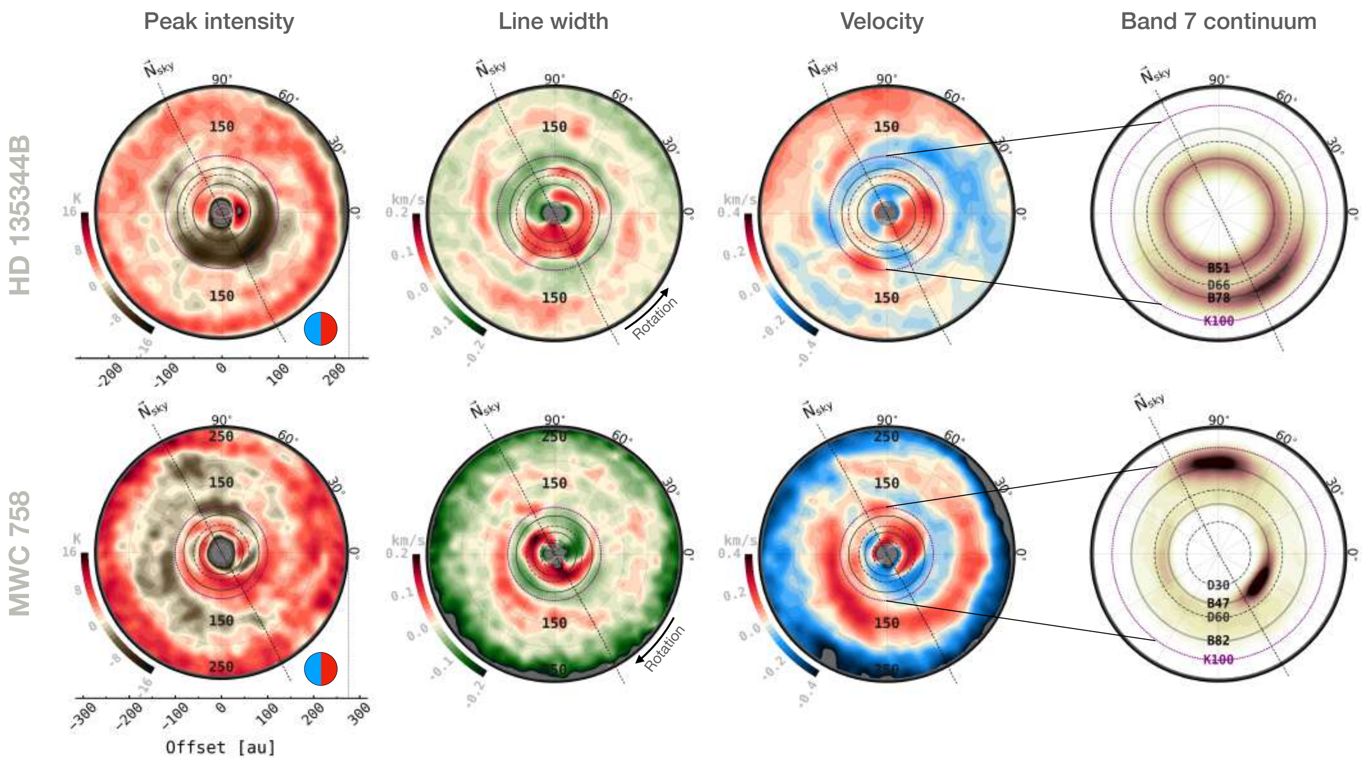

Figure 11. Peak-intensity (left column), line-width (middle left), and velocity (middle right) residuals traced by ^{12}CO $J = 3$ 2, along with band 7 continuum emission (right), from the disks of HD 135344B (top row) and MWC 758 (bottom), deprojected onto each disk's reference frame. In this frame, the vertical axis is aligned with the projected minor axis of the disk on the sky. Also shown is the north axis (where PA = 0) of the sky for reference. The blue/red circle in the bottom right corner of the leftmost panels marks the blueshifted and redshifted sides of each disk. Solid and dashed lines indicate the radial location of millimeter dust rings and gaps, respectively, and the purple dotted lines highlight the orbits of the outermost planet candidates proposed in the literature to explain the observed dust features. These targets exhibit a high degree of substructure in all three types of residuals, suggesting the presence of strong pressure fluctuations and deviations from Keplerian motion.

Doppler flips) that closely overlap with regions of enhanced line broadening. In contrast, MWC 758 is dominated by extended signatures, manifesting as spirals, annular structures, and arcs throughout the different line diagnostics. In the remainder of this section, we focus on the retrieval and interpretation of these features. For applications to the full exoALMA sample, we refer the reader to M. Fukagawa et al. (2026) and M. Benisty et al. (2026), which present a systematic identification and analysis of residual features across all targets.

4.1. Localized Features in HD 135344B

We follow the approach described in Section 3.2 to search for planet candidates associated with localized signatures in the line-width and velocity maps of HD 135344B. In this source, we identify strongly localized line-width peaks and clusters, shown in Figure 12 as circles and crosses, respectively. Two such features, labeled "1" and "2," are detected in ^{12}CO at ($R = 41$ au, $\phi = 36$) and ($R = 73$ au, $\phi = 15$), and in ^{13}CO at ($R = 78$ au, $\phi = 26$), where R denotes the cylindrical radius and ϕ is the azimuthal angle

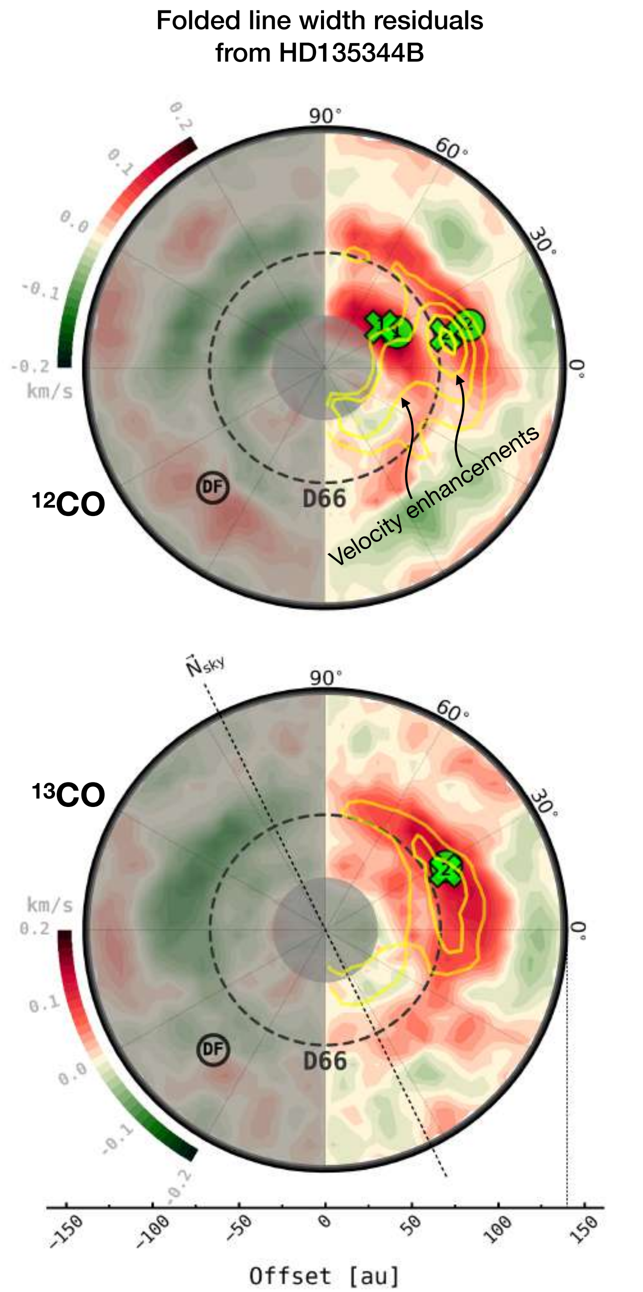

Figure 12. Folded line-width residuals from ^{12}CO and ^{13}CO $J = 3$ 2 emission for the disk of HD 135344B. The region between $R = 30$–90 au in the first quadrant displays significant line-width enhancements in both tracers, indicating perturbations spanning multiple altitudes above the disk midplane, potentially driven by a massive planet. Green circles mark the locations of global peaks, while green crosses represent detected clusters associated with highly localized signals. Yellow contours highlight cospatial peak velocity residuals in the range of +50 to +300 m s^{-1}. The outermost ^{12}CO cluster coincides with both the global velocity peak and the detected cluster in ^{13}CO.

measured from the redshifted major axis in the deprojected disk frame. Although these features dominate the peak extraction, line-width enhancements in 12CO are also observed near the velocity Doppler flip labeled "DF", reported in Section 4.1.1 at (R = 95 au, ϕ = −133). Table 1 summarizes the locations of these planet candidates, together with their sky-projected coordinates relative to the disk center from the best-fit DISCMINER model of A. F. Izquierdo et al. (2025).

Table 1
Planet Candidates Identified in the Disk of HD 135344B, Including Their Locations in Polar and Sky-projected Coordinates

Candidate	R (au)	ϕ (deg)	R (arcsec)	PA (deg)	Tracer
C1	41	36	0.30	278	^{12}CO
C2	73	15	0.54	258	^{12}CO & ^{13}CO
DF	95	−133	0.69	109	^{12}CO & ^{13}CO

Note. See Section 4.1 for details.

The amplitudes of the detected line-width signals in ^{12}CO are 0.18 and 0.13 km s^{-1} for candidates "1" and "2," respectively, and 0.16 km s^{-1} for the ^{13}CO feature associated with candidate "2". Prominent velocity residuals are also found in the same region of the disk (shown as yellow contours), reaching amplitudes of up to 0.26 km s^{-1} in ^{12}CO, and 0.14 km s^{-1} in ^{13}CO. However, these residuals do not form clusters that are significantly more localized than those observed elsewhere in the disk, indicating that velocity perturbations are spatially more extended than the corresponding line-width enhancements. This behavior is fully consistent with the predictions from our massive planet–disk interaction simulations (see, e.g., Figure 3).

A. F. Izquierdo et al. (2023) reported similar localized line broadening traced by CO emission in the disc of HD 163296, spatially coincident with a velocity Doppler flip and chemical anomalies attributed to its circumplanetary region (A. F. Izquierdo et al. 2022, 2026); in the disc of MWC 480, at the radial location of candidate planet-driven buoyancy spirals (R. Teague et al. 2021); and in AS 209, in the region where a circumplanetary disc was proposed based on localized 13CO intensity signals (J. Bae et al 2022).

4.1.1. A Prominent Doppler Flip at R = 95 au

Doppler-flip signatures also serve as indicators of the presence of embedded planets in disks. These features manifest as sharp transitions between negative and positive velocity residuals, arising from the gravitational interaction between the planet and the surrounding gas in its vicinity (e.g., S. Pérez et al. 2018). They also provide valuable diagnostics of the planet mass and orbital parameters and, to a lesser extent, of the local disk viscosity and temperature structure (I. Rabago & Z. Zhu 2021).

In cases with high substructure complexity, where Doppler-flip perturbations are not the strongest but remain visually detectable, as in the disk of HD 135344B, we apply a peak-finding algorithm on gradient residual maps to pinpoint the central location of these signatures. This is illustrated in Figure 24 of the Appendix, where we present azimuthal gradient maps of velocity residuals in ^{12}CO and ^{13}CO. Pluses and minuses overlaid on the reference residual map denote positive and negative peak gradients, respectively, to mark the locations of Doppler flips in the velocity field. Azimuthal gradient peaks with values below 50 m s^{-1} beam^{-1} were excluded from the analysis, retaining only the steepest gradients corresponding to velocity shifts exceeding half the channel spacing of the data per beam. The radial section of the disk where the Doppler-flip signatures overlap in ^{12}CO and ^{13}CO is highlighted. Among the peaks that are cospatial within a beam size (∼20 au at the source distance) for these tracers, three correspond to sequential velocity sign flips centered at

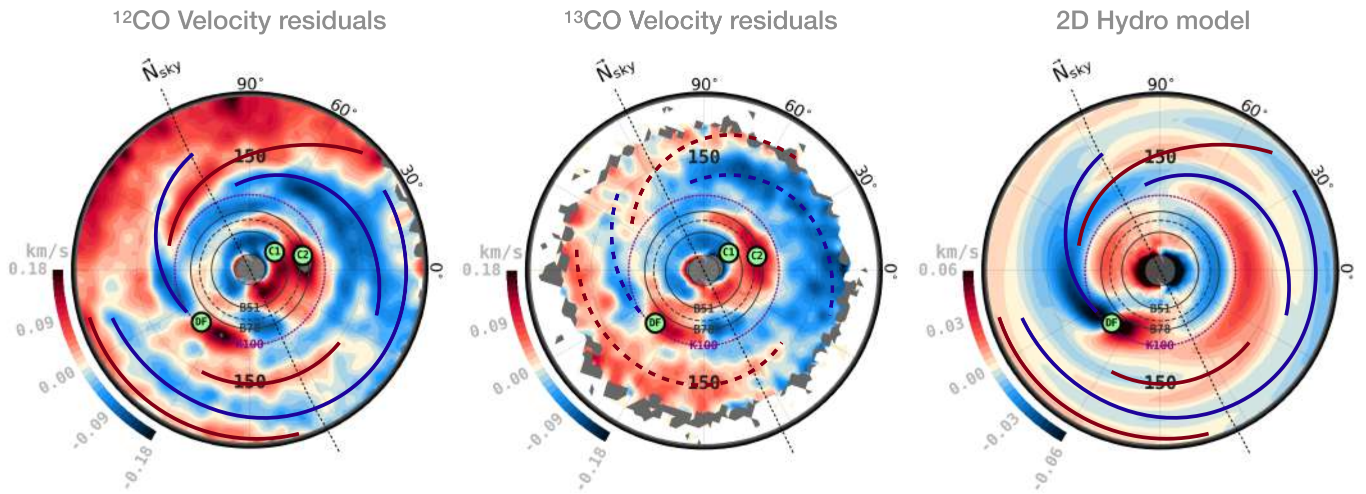

Figure 13. Centroid velocity residuals observed in the ^{12}CO and ^{13}CO data of the HD 135344B disk, compared with a two-dimensional hydrodynamical model tailored to this system. The Doppler flip identified in Section 4.1.1, centered at the DF marker, spatially overlaps in both tracers and is accompanied by large-scale velocity substructures spanning a broad radial and azimuthal extent of the disk. These features are qualitatively reproduced by the hydrodynamical model, generated with the PPDONET neural network introduced by S. Mao et al. (2023) and postprocessed with DISCMINER, assuming a 6 $M_{\rm Jup}$ planet at the center of the Doppler flip, an aspect ratio of 0.075, and an α viscosity of 10^{-2}. The red and blue solid lines overlaid on the model residuals trace the large-scale ^{12}CO signatures, emphasizing the similarity in both the velocity sign flips and the spatial extent of the structures near and far from the planet, despite the simplicity of the adopted model.

$(R, \phi) = (95\,\mathrm{au}, -133\ )$, $(89\,\mathrm{au}, -93\ )$, and $(80\,\mathrm{au}, -60\ )$ in the disk reference frame, and one at $(72\,\mathrm{au}, 24\ )$ cospatial with the line-width clusters and velocity perturbations reported earlier in Figure 12.

We propose the presence of a massive embedded planet at the location of the most prominent Doppler flip, centered at $R = 95$ au and $\phi = -133$. The peak negative-to-positive amplitude of this signal is 0.32   0.02 km s^{-1} in ^{12}CO and 0.24   0.04 km s^{-1} in ^{13}CO, implying a modest decrease toward the disk midplane. Additional evidence supporting this candidate includes a spiral-like structure seen in positive line-width residuals (Figures 11 and 12 , top row) emerging from the location of the Doppler flip, as well as a local minimum in the azimuthally averaged line widths at this orbital separation (Figure 10 in A. F. Izquierdo et al. 2025), which may indicate a surface-density gap traced by reduced line saturation owing to the lower optical depth (A. Hacar et al. 2016; A. F. Izquierdo et al. 2021).

Variations in the amplitude of this velocity feature across lines may provide additional clues about the vertical location and physical mechanism driving the signal. Given that the disk of HD 135344B is close to face-on ($i = -16$), we speculate that a substantial fraction of the observed velocity signals, and their modulation with altitude, are likely shaped by vertical motions. C. Pinte et al. (2019) and I. Rabago & Z. Zhu (2021) found in their simulations that vertical downward velocities are highest near an embedded planet, peaking at approximately one pressure scale height above the midplane. In our proposed scenario, this would imply that ^{12}CO traces gas closer to this elevation than ^{13}CO, suggesting a relatively flat disk compared to the average z/r of the exoALMA sample. Interestingly, this interpretation is consistent with the low z/r values reported for disks with similar radial extents, such as CQ Tau or PDS 66 (see, e.g., Fig. 6 of M. Galloway-Sprietsma et al. 2025). The assumption of a shallow disk to explain the reduction in velocity amplitude toward the midplane could be relaxed, however, if the planet also excites buoyancy resonances. In that case, vertical motions would begin to weaken from even higher elevations (J. Bae et al. 2021).

To further investigate the influence of this planet on the disk structure, we generated a velocity map from hydrodynamical models of planet–disk interaction tailored to this system using the PPDONET neural network (S. Mao et al. 2023). We then subtracted the best-fit Keplerian rotation derived with DISCMINER for this target in A. F. Izquierdo et al. (2025) to obtain velocity residuals. The adopted setup assumes a gas-disk alpha viscosity of 10^{-2}, an aspect ratio of 0.075, and a 6 $M_{\rm Jup}$ planet located at the center of the Doppler flip,[31] consistent with previous models used to reproduce the spiral arms observed in scattered light (see Section 5.1 for discussion).

Figure 13 compares the residuals from the ^{12}CO and ^{13}CO data with those predicted by the hydrodynamical model. In addition to the Doppler-flip signature, the model exhibits large-scale substructures, including arcs and spiral-like patterns, that closely resemble those observed in ^{12}CO (traced by the solid blue and red lines) and in ^{13}CO. The consistency of the velocity patterns across different molecular lines suggests that the observed substructures share a common origin and that the associated perturbations propagate over multiple scale heights within the disk's vertical structure.

We note, however, that although the overall dynamical structure of the disk is well reproduced by invoking this planet, the amplitude of the model residuals is lower by a factor of ~2–3 compared to the observations. This discrepancy may be mitigated by incorporating vertical motions and temperature gradients into the models, which are expected to enhance the planet-driven velocity features (e.g., J. Bae et al. 2021) without requiring a prohibitively high planet mass that would otherwise conflict with direct-imaging constraints ruling out planets more massive than 3 $M_{\rm Jup}$ at the orbital radius of the Doppler flip (G. Cugno et al. 2024). Full three-dimensional

[31] These parameters were not derived from a formal best-fit procedure but were manually adjusted to qualitatively reproduce the localized and large-scale features observed in the data. Moreover, because the neural network does not account for vertical motions or vertically stratified temperature structures, the adopted parameters may not correspond to the optimal physical properties required to reproduce the observed disk kinematics.

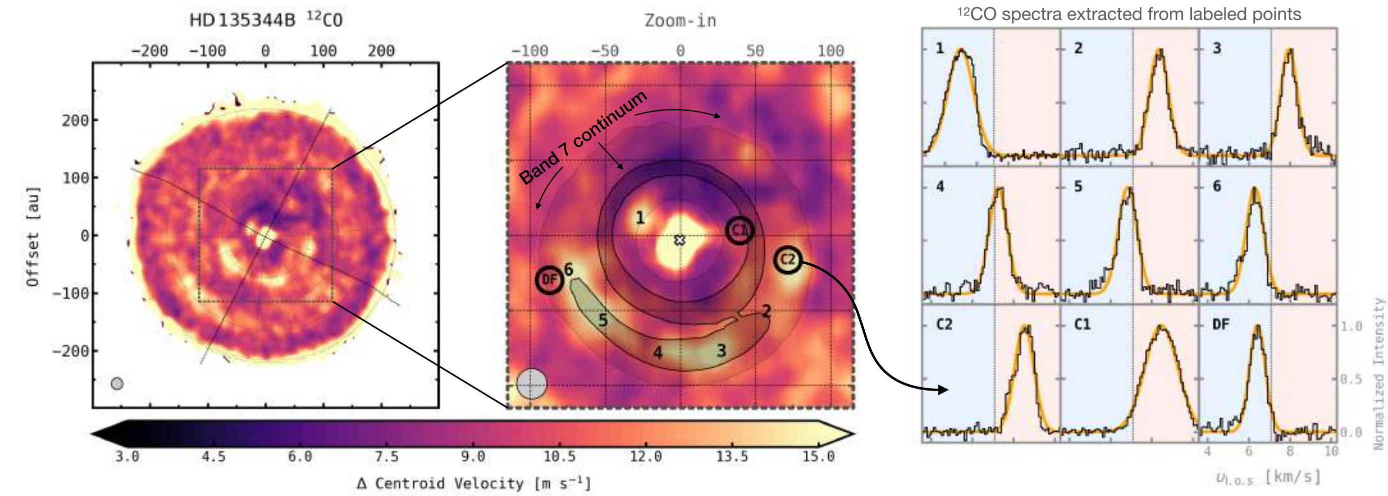

Figure 14. Statistical uncertainties in centroid velocities derived from Gaussian fits to the ^{12}CO $J = 3$ 2 line profiles for the disk of HD 135344B. The zoom-in panel highlights localized signals near the millimeter continuum crescent (outlined by black contours to the south), around the proposed planet associated with line-width clusters and velocity peaks at $R = 73$ au (denoted by the C2 circle), and near the planet candidate linked to the velocity Doppler-flip signature at $R = 95$ au (marked by the DF circle). In the rightmost panels, spectra extracted from the numbered points in the middle panel illustrate the asymmetric line profiles responsible for the increased uncertainties. These morphologies suggest the presence of spatially unresolved velocity flows and are reminiscent of the line shapes predicted by synthetic observations of planet–disk interaction simulations (see Section 3.3).

simulations are therefore essential to reliably constrain the masses of embedded planets from kinematic signatures, particularly in low-inclination disks.

4.1.2. Line Asymmetries around Line-width Signals

We also find evidence for asymmetric line profiles at the locations of the outermost line-width clusters detected in ^{12}CO and ^{13}CO, consistent with the predictions from our planet–disk interaction simulations discussed in Section 3.3. Figure 14 presents a map of 1σ statistical uncertainties in centroid velocities derived from Gaussian fits to the ^{12}CO line emission of this source. Typical uncertainties are $\sim$10 m s^{-1}, with enhanced values partially tracing the millimeter continuum crescent and localized increases around the line-width cluster at $R = 73$ au and near the Doppler flip identified at $R = 95$ au. An additional localized feature is found interior to the millimeter ring B51, at $R = 30$ au.

To illustrate the origin of these elevated uncertainties, we extracted spectra at the positions of the outer line-width cluster and at pixels cospatial with the millimeter crescent. These profiles exhibit clear asymmetries relative to their line centroids and, in the most prominent cases, appear double-peaked, indicating the presence of multiple overlapping velocity components. In all cases, however, the asymmetries favor downward flows, consistent with predictions from our planet–disk simulations (see Figures 9 and 22). Near the outer edge of the disk, at $R \sim 170$ au, elevated uncertainties also align with the spiral structure identified in line-width residuals (Figure 11), suggesting spatially unresolved and asymmetric velocity flows along this feature as well.

Figure 15 summarizes the localized signatures identified in HD 135344B. In Section 5, we examine the possible connection between these candidate planet-driven perturbations and the dust substructures revealed by millimeter and near-infrared continuum observations of this source.

4.2. Large-scale Signatures in MWC 758

The disk of MWC 758 exhibits prominent spiral-like signatures across all three residual diagnostics. To identify and quantify these perturbations, we employ the FILFINDER code (E. W. Koch & E. W. Rosolowsky 2015), which applies an adaptive thresholding algorithm to isolate pixels belonging to coherent substructures (referred to as filaments) over a wide dynamic range in the observable of interest. Each detected substructure is assigned a two-dimensional mask, which is subsequently reduced to a one-dimensional skeleton via a medial axis transform (first introduced by H. Blum 1967) to serve as a shape descriptor. The resulting medial axes are then used to characterize the morphology and spatial configuration of the filaments (see, e.g., A. F. Izquierdo et al. 2022, for an application to the disk kinematics of HD 163296). For this purpose, we consider several geometric descriptors provided by FILFINDER, including filament length, width, and orientation.

The results of this analysis are presented in Figure 25 in the Appendix, which shows the filaments identified in the ^{12}CO velocity residuals, together with their measured pitch angles and projected widths. We find that the longest velocity feature, highlighted in cyan across all panels, exhibits a nearly uniform pitch angle of $\sim 0\overset{\circ}{.}3$ at all radii, forming an annular pattern that coherently traces blueshifted velocities consistent with outflowing material in the outer disk regions (see M. Benisty et al. 2026, for details). In contrast, the larger and radially varying pitch angles retrieved for the inner filaments suggest that these correspond to nonaxisymmetric substructures forming spiral patterns, possibly driven by embedded companions (see Section 5). We also find that the two outermost filaments are spatially resolved, with an average FWHM of $\sim$1.5 beams measured perpendicular to their medial axes. The outermost blueshifted filament, however, may extend beyond this width in regions of lower SNR that were excluded from the analysis.

The velocity spirals manifest as coherent redshifted and blueshifted patterns extending over more than $\sim$270 in azimuth, without sign reversals across the disk's minor and major axes. As illustrated in Figure 2, this behavior suggests that the signatures are likely dominated by downward and upward vertical motions, respectively.

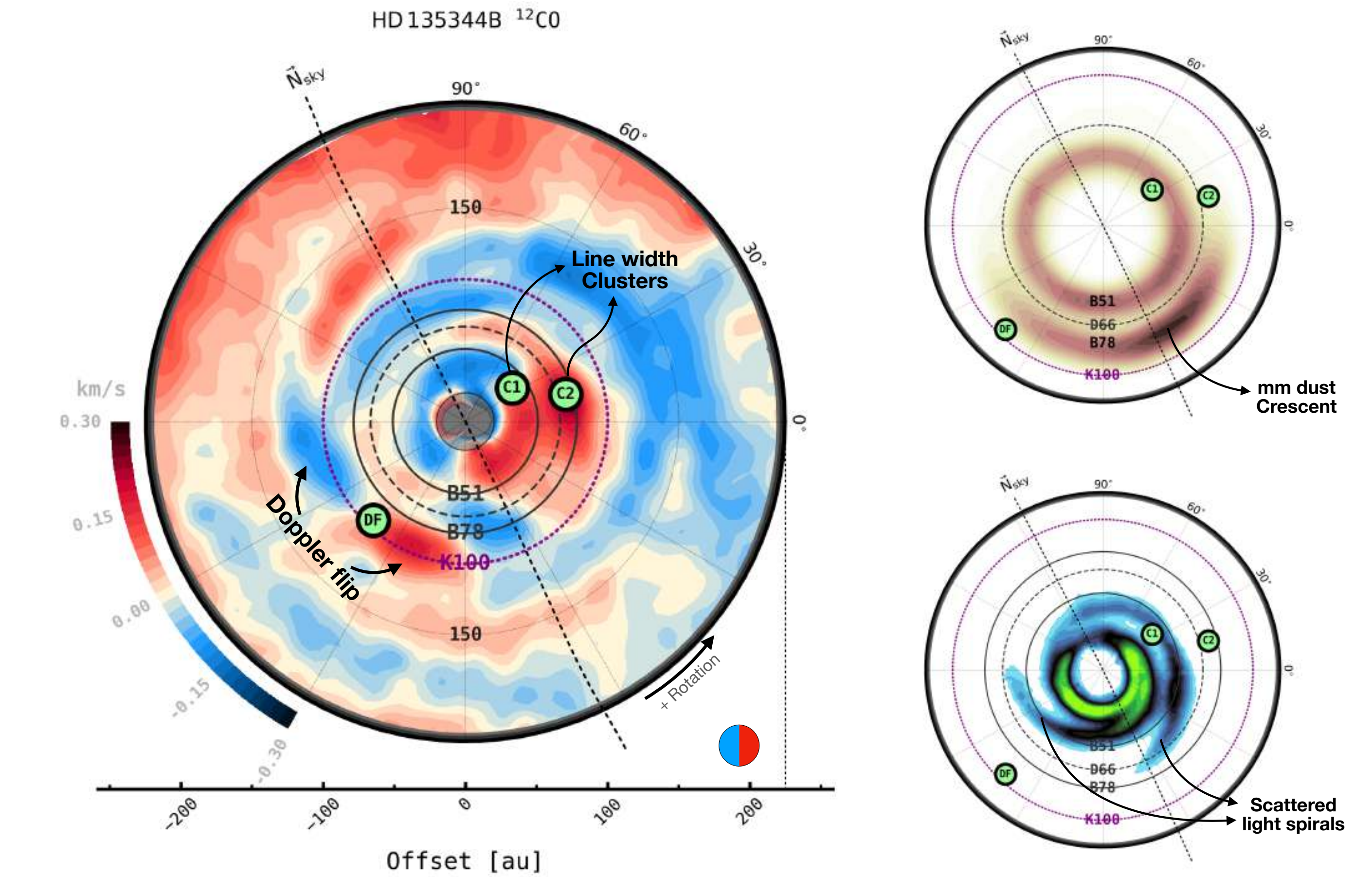

Figure 15. Deprojected view of velocity and dust substructures in the disk of HD 135344B. Left: ^{12}CO $J = 3$ 2 velocity residuals illustrating deviations from Keplerian rotation in the gas disk. Bottom right: VLT/SPHERE near-infrared observations (T. Stolker et al. 2016) probing scattered light from micron-sized dust grains. Top right: ALMA band 7 continuum observations (P. Curone et al. 2025; R. Teague et al. 2025) tracing thermal emission from millimeter-sized dust grains. Solid and dashed lines mark the radial locations of peaks and troughs in the millimeter continuum, while the purple dotted K100 line indicates the orbital radius of the planet candidate proposed by R. Dong et al. (2015) and J. Bae et al. (2016) to reproduce the near-infrared spirals and the millimeter dust crescent. The green circles indicate the locations of the Doppler flip and line-width clusters identified in ^{12}CO and ^{13}CO in this work, potentially associated with embedded planets.

To further characterize the morphology of these substructures, we fitted logarithmic ($r = ae^{b\phi}$) and linear ($r = a + b\phi$) spiral models to their medial axes using SCIPY's least-squares minimization algorithm. Figure 16 shows the resulting analytic spirals overlaid on the velocity, line-width, and peak-intensity residual maps, with the best-fit parameters listed in Table 2. Both logarithmic and linear prescriptions reproduce the overall geometry of the velocity spirals reasonably well. However, the extrapolated logarithmic spiral provides a better match to velocity and intensity features in the inner disk, particularly near the millimeter dust crescents B47 and B82, which the linear model fails to capture.

This analysis also demonstrates that the redshifted velocity spiral spatially coincides with elongated regions of enhanced line width, regardless of the adopted fitting prescription. The absence of corresponding temperature increases along this spiral, as traced by the ^{12}CO peak-intensity residuals, indicates that the observed line broadening most likely arises from unresolved velocity flows, high optical depths, or a combination of both, rather than from shock or radiative heating of the gas.

5. Discussion

5.1. Planets in the Disk of HD 135344B

As illustrated in Figure 15, all kinematic and line-width signatures identified in the disk of HD 135344B are located near the dust ring (B51), gap (D66), and azimuthal dust trap (B78) observed in the millimeter continuum (N. van der Marel et al. 2016; P. Cazzoletti et al. 2018; P. Curone et al. 2025), suggesting a strong connection between these substructures and pressure modulations potentially induced by embedded companions. Notably, the same radial region of the disk hosts a nearly symmetric two-armed spiral structure observed in the near-infrared (T. Muto et al. 2012; A. Garufi et al. 2013; T. Stolker et al. 2016; B. B. Ren et al. 2023; F. Maio et al. 2025), consistent with expectations from tidal interactions between disks and planets (e.g., R. Dong et al. 2015; J. Bae et al. 2016; C. Baruteau et al. 2019). From a kinematic perspective, and based on the small and large-scale signatures identified in Section 4.1, we propose three plausible locations for embedded planets in this disk.

First, a planet candidate (C2) at a radial separation of $R = 73$ au, near the inner edge of the millimeter dust asymmetry B78 and azimuthally within the first half of the first quadrant of the disk, centered at $\phi = 15$ as inferred by our clustering analysis (or $R = 0''.54$, PA = 258 in projected sky coordinates). This object would produce line broadening and blueshifted asymmetries, as well as strong velocity perturbations at different heights above the midplane traced by ^{12}CO and ^{13}CO (Figures 12, 13, and 14). Its radial location is close to that of the planet proposed by C. Xie et al. (2024) at an

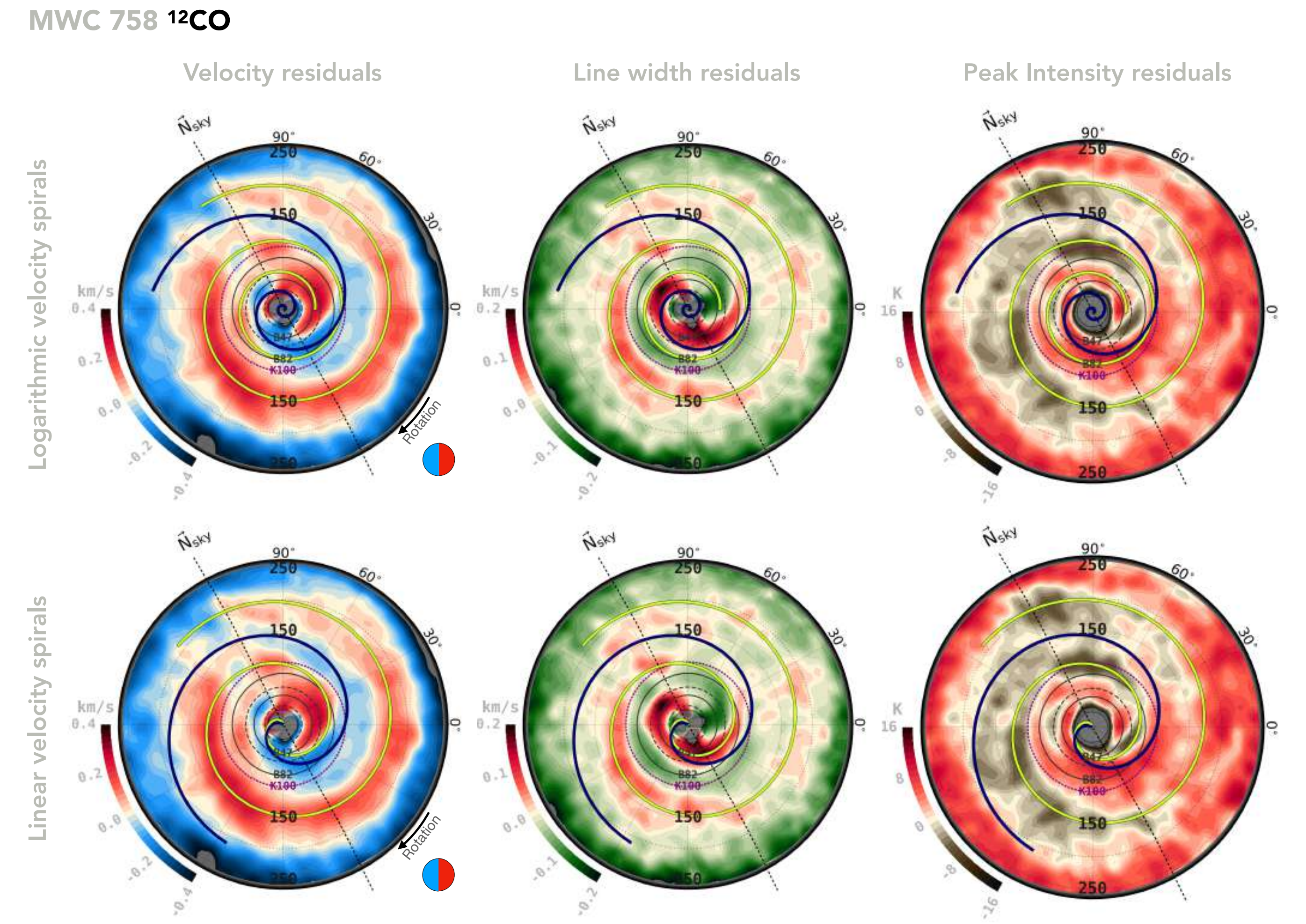

Figure 16. Logarithmic ($r = ae^{b\phi}$, top) and linear ($r = a + b\phi$, bottom) spiral models fitted to the spirals identified in ^{12}CO velocity residuals for the disk of MWC 758, overlaid on the velocity (left), line-width (middle), and peak-intensity (right) residual maps. Table 2 summarizes the best-fit parameters for the spirals. While both prescriptions reproduce the overall morphology of the outer signatures in velocity and line width, the logarithmic model additionally captures the inner features in velocity and peak intensity near the radial locations of the millimeter dust crescents B47 and B82.

Table 2
Best-fit Parameters for the Spiral Fits to the Velocity Structures Traced by ^{12}CO $J = 3$ 2 Emission in the Disk of MWC 758

Type	Component	a(au)		b	
Logarithmic ($r = ae^{b\phi}$)	Positive	170.0	1.1	5°.5	0°.3
	Negative	95.8	2.3	15°.1	1°.4
Linear ($r = a + b\phi$)	Positive	171.7	1.1	15.8	0.6
	Negative	99.4	1.9	26.2	1.7

Note. Parameter b in the linear fit is expressed in units of au rad^{-1}.

orbital radius of $R = 66$ au to explain the pattern speed of the near-infrared spirals[32] observed in this source (Figure 15).

The second candidate (C1) corresponds to a closer-i planet located at $R = 41$ au and $\phi = 36$ (or $R = 0\farcs30$, PA = 278), interior to the inner dust ring B47, and possibly responsible for the localized line broadening in the disk upper layers traced by ^{12}CO (Figure 12). However, the absence of ^{12}CO line asymmetries (Figure 14) and the only moderate broadening detected in ^{13}CO at this location suggest that, if such a planet exists, it is likely less massive than 1.6 $M_{\rm Jup}$ (i.e., <0.1% of the stellar mass), as predicted by our planet–disk interaction models. Alternatively, these signatures may reflect outlier perturbations from an even more interior planet that cannot be robustly constrained due to beam smearing at small radii, given the finite angular resolution of our data (∼20 au at the source distance). This scenario would be broadly consistent with the findings of F. Maio et al. (2025), who propose a 2 $M_{\rm Jup}$ planet to explain a compact infrared intensity signal at an orbital radius of 29 au and an azimuth of $\phi = 31$, which overlaps in azimuth with the ^{12}CO line-width feature reported here, though at a slightly smaller radial separation.

This also aligns with A. Garufi et al. (2013) and N. van der Marel et al. (2016), who suggested that a massive planet at ∼30 au could generate the pressure maximum responsible for the millimeter dust ring B51. N. van der Marel et al. (2016) further proposed that this inner pressure bump could induce a secondary pressure maximum at larger radii, triggering a vortex via the Rossby wave instability and leading to the formation of the millimeter dust crescent B78 as an

[32] The reference Keplerian velocity adopted in the spiral-pattern analysis is consistent with that used in this work, as C. Xie et al. (2024) assumed a nearly identical stellar mass (1.6 $M_\odot$) and disk inclination (16°.7), matching the values independently inferred from the disk kinematics in A. F. Izquierdo et al. (2025).

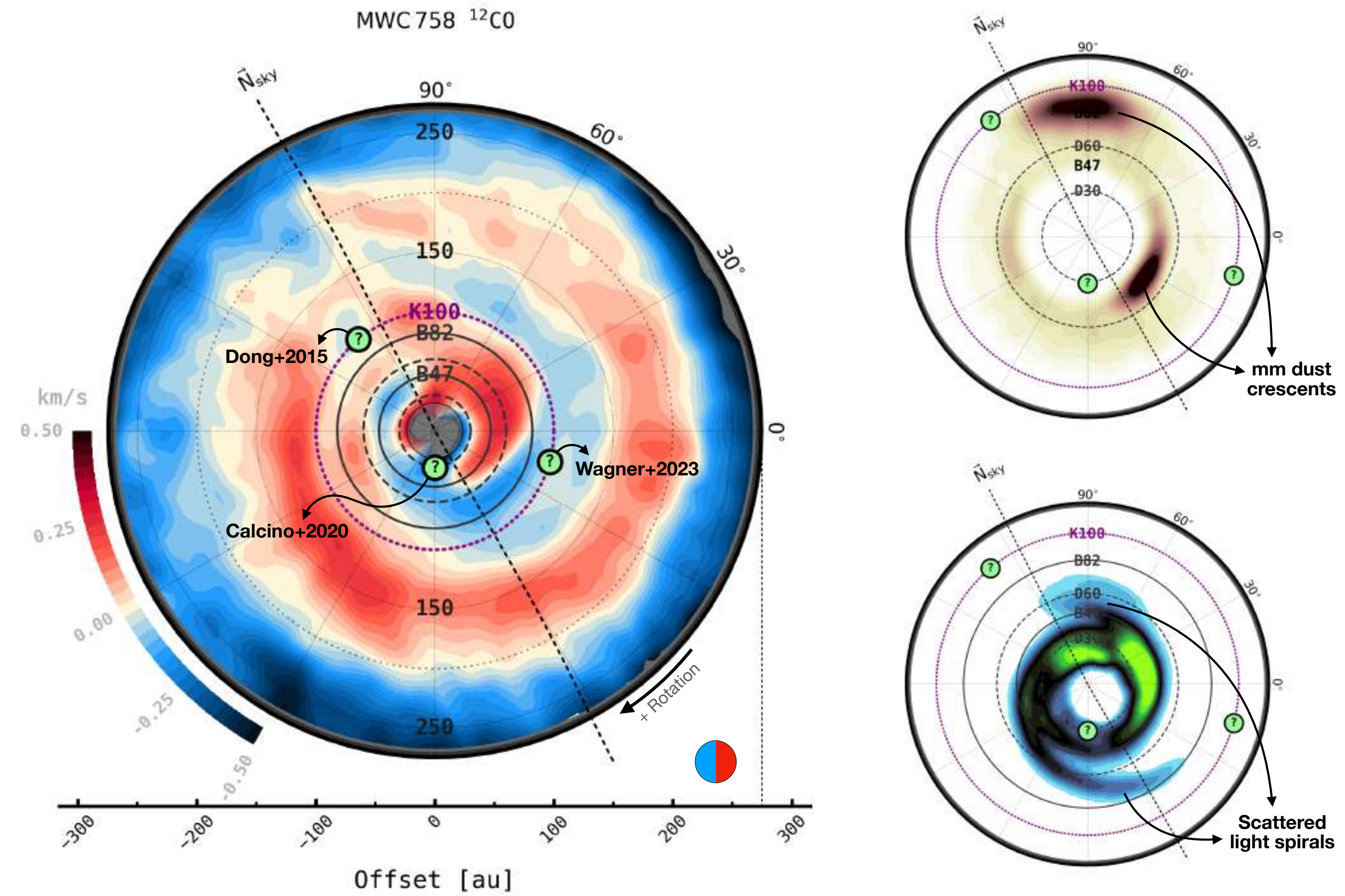

Figure 17. Deprojected view of velocity and dust substructures in the disk of MWC 758. *Left*: ^{12}CO $J = 3$ 2 velocity residuals illustrating deviations from Keplerian rotation in the gas disk. Bottom right: VLT/SPHERE near-infrared observations (M. Benisty et al. 2015) probing scattered light from micron-sized dust grains. Top right: ALMA band 7 continuum observations (P. Curone et al. 2025; R. Teague et al. 2025) tracing thermal emission from millimeter-sized dust grains. Solid and dashed lines mark the radial locations of peaks and troughs in the millimeter continuum, while the purple dotted K100 line indicates the orbital radius of the giant planet proposed by K. Wagner et al. (2023) based on a compact signal identified at infrared wavelengths. The green circles indicate the locations of selected planet candidates reported in the literature to explain the observed dust substructures.

asymmetric dust trap. In their interpretation, one of the spiral arms observed in scattered light would originate from the vortex overdensity, while the other would be driven by the inner planet candidate. Interestingly, P. Cazzoletti et al. (2018) argued that the vortex alone could potentially excite the entire spiral structure, having accumulated sufficient mass (up to a few Jupiter masses) to perturb the disk kinematics. Such a scenario could account for the enhanced line widths (Figure 11) and spectral asymmetries (Figure 14) observed around the dust crescent. This is also partly consistent with the findings of L. Wölfer et al. (2025), who show that the kinematic pattern near the millimeter crescent resembles that expected from a vortex, although it cannot, on its own, reproduce the more extended features.

Finally, we identify a third planet candidate (DF) associated with a Doppler-flip velocity signature in the third quadrant of the disk at $R = 95$ au and $\phi = -133$ (or $R = 0\farcs69$, PA = 109), detected in both ^{12}CO and ^{13}CO velocity maps. This planet may also be responsible for a surface-density dip traced by reduced azimuthally averaged line widths at the same orbital radius (see Figure 10 of A. F. Izquierdo et al. 2025, and Figure 20 of this work). Moreover, its inferred location is in excellent agreement with the planet proposed by R. Dong et al. (2015) and J. Bae et al. (2016) to explain both the two-armed spiral observed in scattered light and the millimeter dust crescent B78.

Notably, this Doppler flip is intersected by the innermost tip of a large-scale line-width spiral extending between ∼100 and 200 au (see Figure 11, top row), and may therefore be associated with the spiral density waves driven by the planet. The absence of elevated temperatures along this spiral further suggests a nonthermal origin, likely associated with enhanced turbulence, or more generally, unresolved velocity flows, increased optical depth, or a combination of both. This complements the findings of S. Casassus et al. (2021), who reported turbulent spiral features traced by ^{12}CO $J = 2$ 1 emission in this source, albeit located closer to the inner disk and spatially coincident with the near-infrared spirals.

5.2. Origin of the Spiral Structures in MWC 758

Previous studies of the disk around MWC 758 have revealed spiral structures traced by scattered light (C. A. Grady et al. 2013; M. Benisty et al. 2015) and molecular-line emission (Y. Boehler et al. 2018), as well as pronounced asymmetries in the millimeter continuum (R. Dong et al. 2018) within the inner ∼100 au. From a kinematic perspective, this source stands out within our sample due to its prominent velocity and line-width spirals, which extend from the inner disk regions out to ∼200 au in both ^{12}CO and ^{13}CO lines. Figure 17 illustrates the spatial configuration of these velocity substructures together with the near-infrared spirals and the locations of the millimeter continuum crescents.

Two main scenarios involving embedded companions have been proposed to explain the origin of the continuum substructures in this source. The first invokes the presence of at least one massive planet or stellar companion inside the millimeter dust cavity ($R_p < 49$ au), with the near-infrared two-armed spirals located exterior to the companion's orbit. The second scenario proposes a massive planet outside the cavity, capable of exciting the spiral's interior to its orbit.

Within the first group, J. Calcino et al. (2020) showed that a massive planet on an eccentric orbit ($e = 0.4$) with a semimajor axis of 33.5 au—close to the pointlike source reported by M. Reggiani et al. (2018) at ∼20 au—can independently reproduce the two-armed spiral structure. In the second group, R. Dong et al. (2015) demonstrated that a single massive planet ($M_p/M_\star = 6 \times 10^{-3}$) located at $R_p \sim 100$ au could similarly excite the observed spirals. More recently, K. Wagner et al. (2023) reported a localized infrared intensity signal at a similar orbital radius, though on the opposite side of the disk, spatially connected to the southern near-infrared spiral arm. While such a planet would be broadly consistent with the line-width minimum identified in our data after azimuthal averaging at $R \sim 90$ au, the absence of a localized velocity or line-width perturbation at this orbital radius disfavors the presence of a high-mass companion.

By measuring the pattern speed of the near-infrared spirals, B. Ren et al. (2020) also proposed the presence of an outer planet, though at a larger orbital radius of 172 au. Since that study adopted higher values for both the stellar mass and disk inclination ($M_\star = 1.9\,M_\odot$ and $i = 21$) than those inferred from our kinematic analysis ($M_\star = 1.4\,M_\odot$ and $i = 19\overset{\circ}{.}4$; A. F. Izquierdo et al. 2025), the corresponding planet location would shift to smaller radii when recalculated using our updated parameters. Similarly, the absence of localized perturbations in these outer regions argues against the presence of a high-mass planet at such separations.

Turning to the kinematical features revealed in our data, vertical motions appear to play a dominant role in shaping the tightly wound velocity spirals observed in this source (Figure 17). This effect is likely enhanced by the nearly face-on orientation of the disk, in which radial and azimuthal velocity components are strongly suppressed by projection effects. If these spirals are of planetary origin and intrinsically dominated by vertical motions, their morphology and velocity structure would be broadly consistent with spiral waves launched at buoyancy resonances by an embedded companion (J. Bae et al. 2021). Spirals driven at Lindblad resonances by an inner massive planet could, in principle, account for the large pitch angles traced by the scattered-light spirals in the inner disk, while also reproducing the gradual decrease in pitch angle of the outer velocity spirals with radius (<10 ; see Figure 25). Alternatively, a hybrid scenario involving at least one inner massive planet ($R_p < 40$ au) responsible for the large-pitch spirals in the inner disk, and an outer planet ($R_p \sim 100$ au) driving the tightly wound spirals in the outer regions could explain the observations. A similar two-planet configuration was proposed by C. Baruteau et al. (2019), who invoked a Jupiter-mass planet at 35 au, and a companion 5 times more massive at 140 au to simultaneously explain the scattered-light spirals and the two compact crescents in the millimeter continuum.

Another scenario consistent with the observed vertical spiral motions involves an eccentric circumstellar disk induced by a substellar companion in the innermost regions of the system. E. Ragusa et al. (2024) showed that a companion with a mass of about 10% that of the central star can excite moderate eccentricities in the outer disk ($e \lesssim 0.2$), which in turn generate $m = 1$ blueshifted and redshifted spiral patterns in the vertical velocity component, closely resembling the spiral structures observed in MWC 758. This interpretation is further supported by the measurable eccentricity of the dust cavity in this source ($e \sim 0.1$ R. Dong et al. 2018), as well as by the comparable amplitudes of the vertical motions predicted in eccentric-disk models (∼0.4 km s^{-1}) and those inferred from our velocity spirals (∼0.3 km s^{-1}). Such large vertical velocities are difficult to reproduce via the planet-buoyancy spirals in the outer disk without invoking a very massive planet (J. Bae et al. 2021), making the eccentric-disk scenario one of the most compelling explanations for the observed features. We refer the reader to M. Benisty et al. (2026) for a broader discussion of vertical motions across the exoALMA sample.

An alternative explanation that does not necessarily require embedded companions was recently proposed by A. J. Winter et al. (2025), who demonstrated that the observed $m = 1$ spiral structures in MWC 758 and other exoALMA targets can arise from moderately warped disk geometries. In these models, small radial variations of only a few degrees in inclination and position angle relative to the mean disk orientation can produce azimuthal asymmetries in the projected Keplerian rotation that closely mimic the spiral kinematic patterns observed in this system.

6. Conclusions

In this work, we present a tomographic analysis of molecular-line properties designed to extract and characterize gas substructures in protoplanetary disks observed with ALMA. We first apply this methodology to synthetic observations of planet–disk interaction and disk-instability simulations to evaluate the detectability of localized substructures and line-profile perturbations driven by these mechanisms. We then apply the same framework on exoALMA CO observations of the disks around HD 135344B and MWC 758, where a variety of dust substructures have long been associated with planet–disk interactions. Our main findings are summarized as follows:

1. Through synthetic observations of planet–disk interaction simulations, we identify a correlation between the location of embedded planets and localized line broadening in the disk (Figure 3). Using line-width enhancements as tracers of planets offers significant advantages over kinematic analyses based solely on line-centroid perturbations, as this observable is largely insensitive to the planet's azimuthal location and provides a higher degree of spatial clustering (Figures 4, 6, and 7).
2. Planets with masses greater than 0.2% of the stellar mass (e.g., $2\,M_{\rm Jup}$ for a $1\,M_\odot$ star) can be robustly detected through line-broadening signatures in disks of moderate inclination ($i < 45$) under fiducial exoALMA observational setups. Importantly, achieving a high SNR at the

planet's location is more critical for detection than high angular or spectral resolution (Figures 5, 6, and 7). Increasing the SNR by a factor of ∼8 (e.g., by degrading the beam size from 0.″15 to 0.″3) enables the detection of planets with masses as low as 0.1% of the stellar mass, which would otherwise remain undetected even in disks at low inclinations ($i < 30$).

3. Although disk instabilities can also produce localized velocity and line-width perturbations (Figure 8), they can be distinguished from planet-driven signals by examining the morphology of the corresponding line profiles. Broadened optically thick lines in the vicinity of an embedded planet are asymmetric around the line centroid and exhibit an intensity deficit toward blueshifted velocities, consistent with partially resolved meridional flows preferentially traced from the upper disk surface. In contrast, line broadening associated with disk instabilities is comparatively more isotropic, with intensity distributions concentrated closer to the line centroid (Figures 9 and 10).
4. We identify evidence for the presence of unseen planets in the disk of HD 135344B. Based on the analysis of peak and clustered perturbations in velocity and line-width residuals, we propose three candidate locations for these companions. The first corresponds to a planet at $R = 73$ au and $\phi = 15$, responsible for the observed line broadening across multiple vertical layers of the disk and exhibiting line asymmetries consistent with our planet–disk synthetic observations. The second is a more interior planet at $R = 41$ au and $\phi = 36$, triggering increased velocity dispersions in the disk's upper layers (Figure 12). The third candidate lies exterior to the continuum substructures and induces a Doppler-flip signature centered at $R = 95$ au and $\phi = -133$, accompanied by a spiral-like line-width perturbation and large-scale velocity structures qualitatively reproduced by a PPDONET hydrodynamical model (Figure 13). While these companions have been previously invoked to explain the substructures observed in the dust continuum emission, this work provides the first gas-based evidence supporting their presence (see Figure 15 for a summary).
5. The disk of MWC 758 is dominated by large-scale perturbations in the form of spiral structures across all line diagnostics. The velocity spirals are tightly wound in the outer disk and spatially coincide with regions of enhanced line broadening, indicative of unresolved velocity flows or increased optical depths (Figure 16). The most prominent spiral exhibits velocity amplitudes of ∼0.2–0.3 km s^{-1}, predominantly shaped by downward vertical motions, with a weaker interior blueshifted counterpart consistent with upward flows. Although a massive planet located exterior to the dust continuum substructures could, in principle, generate a similar velocity spiral, we do not identify any significantly localized perturbation that could be attributed to such a companion. Instead, scenarios involving a warped outer disk or a substellar object in the inner regions provide a more natural explanation for both the observed spiral velocities and the absence of localized signatures (see Figure 17 for a summary).

Acknowledgments

We thank the anonymous referee for the constructive comments and suggestions, which greatly improved the quality of this work. This Letter makes use of the following ALMA data: ADS/JAO.ALMA#2021.1.01123.L. ALMA is a partnership of ESO (representing its member states), NSF (USA) and NINS (Japan), together with NRC (Canada), MOST and ASIAA (Taiwan), and KASI (Republic of Korea), in cooperation with the Republic of Chile. The Joint ALMA Observatory is operated by ESO, AUI/NRAO, and NAOJ. The National Radio Astronomy Observatory is a facility of the National Science Foundation operated under cooperative agreement by Associated Universities, Inc. We thank the North American ALMA Science Center (NAASC) for their generous support, including providing computing facilities and financial support for student attendance at workshops and publications. Support for AFI was provided by NASA through the NASA Hubble Fellowship grant No. HST-HF2-51532.001-A awarded by the Space Telescope Science Institute, which is operated by the Association of Universities for Research in Astronomy, Inc., for NASA, under contract NAS5-26555. J.B. acknowledges support from NASA XRP grant No. 80NSSC23K1312. S.F. is funded by the European Union (ERC, UNVEIL, 101076613) and acknowledges financial contribution from PRIN-MUR 2022YP5ACE. E.F.v.D acknowledges support from the ERC grant 101019751 MOLDISK. M.B., J.S., and D.F. have received funding from the European Research Council (ERC) under the European Union's Horizon 2020 research and innovation program (PROTOPLANETS, grant agreement No. 101002188). P.C. and L.T. acknowledge support by the Italian Ministero dell'Istruzione, Università e Ricerca through the grant Progetti Premiali 2012—iALMA (CUP C52I13000140001) and by the ANID BASAL project FB210003. N.C. has received funding from the European Research Council (ERC) under the European Union Horizon Europe research and innovation program (grant agreement No. 101042275, project Stellar-MADE). M. Flock has received funding from the European Research Council (ERC) under the European Union's Horizon 2020 research and innovation program (grant agreement No. 757957). M. Fukagawa is supported by a grant-in-Aid from the Japan Society for the Promotion of Science (KAKENHI: No. JP22H01274). C.H. acknowledges support from NSF AAG grant No. 2407679. J.D.I. acknowledges support from an STFC Ernest Rutherford Fellowship (ST/W004119/1) and a University Academic Fellowship from the University of Leeds. AI acknowledges support from the National Aeronautics and Space Administration under grant No. 80NSSC18K0828. G.L. has received funding from the European Union's Horizon 2020 research and innovation program under the Marie Sklodowska-Curie grant agreement No. 823823 (DUSTBUSTERS), from PRIN-MUR 20228JPA3A, and the European Union Next Generation EU, CUP: G53D23000870006. C.L. has received funding from the European Union's Horizon 2020 research and innovation program under the Marie Sklodowska-Curie grant agreement No. 823823 (DUSTBUSTERS) and by the UK Science and Technology research Council (STFC) via the consolidated grant ST/W000997/1. F.M. has received funding from the European Research Council (ERC) under the European Union's Horizon Europe research and innovation program (grant agreement No. 101053020, project Dust2Planets). C.P. acknowledges Australian Research Council funding via FT170100040, DP18010423, DP220103767, and DP240103290. D.P. acknowledges Australian Research Council funding via DP18010423, DP220103767, and DP240103290. G.R. acknowledges funding from the Fondazione Cariplo, grant No. 2022-1217, and the European Research Council (ERC) under the European Union's Horizon Europe Research & Innovation Programme under grant agreement No. 101039651 (DiscEvol). A.J.W. has received funding from the European Union's Horizon 2020 research and innovation program under the Marie Sklodowska-Curie grant agreement No. 101104656. Support for B.Z. was provided by The Brinson Foundation. This work was partly supported by the Deutsche Forschungsgemeinschaft (DFG; German Research Foundation)—Ref. No. 325594231 FOR 2634/2 TE 1024/2-1, and by the DFG Cluster of Excellence Origins (www.origins-cluster.de). This project has received funding from the European Research Council (ERC) via the ERC Synergy Grant ECOGAL (grant 855130). Views and opinions expressed by ERC-funded scientists are, however, those of the author(s) only and do not necessarily reflect those of the European Union or the European Research Council. Neither the European Union nor the granting authority can be held responsible for them.

Software: ASTROPY (Astropy Collaboration et al. 2022), BETTERMOMENTS (R. Teague & D. Foreman-Mackey 2018), CASA (T. CASA et al. 2022), CMASHER (E. van der Velden 2020), DISCMINER (A. F. Izquierdo et al. 2021), EMCEE (D. Foreman-Mackey et al. 2013), MATPLOTLIB (J. D. Hunter 2007), NUMPY (C. R. Harris et al. 2020), SCIKIT-IMAGE (S. van der Walt et al. 2014), SCIPY (P. Virtanen et al. 2020), RADIO-BEAM (E. Koch et al. 2021), SPECTRAL-CUBE (A. Ginsburg et al. 2019).

Appendix
Supporting Figures

Here we provide complementary figures that support the results presented in the main text. Figure 18 illustrates selected ^{12}CO channel maps from the synthetic observations of the planet-disc interaction and disc-instability simulations introduced in Section 3. Figure 19 presents azimuthal profiles of projected velocity components from planet-disc interaction simulations, demonstrating how the constructive or destructive overlap of velocities can induce strong signals in this observable away from the planet location. Figure 20 summarizes the key line diagnostics used to distinguish planet-driven signatures in velocity or line-width residual maps. Figure 21 presents the detection score (defined in Section 3.2.1) for planet-driven velocity peaks, complementing the scores based on line-width enhancements (Figure 5). Figure 22 illustrates edge-on slices of the vertical velocity component from planet-disc interaction simulations with planet masses of 0.1 and 0.2% of the stellar mass. This figure demonstrates that converging downward flows are localized to the planet's vicinity and are responsible for the line asymmetries discussed in Section 3.3. Figure 23 shows the absence of line asymmetries in optically thin emission, where planet-driven flows influence the line profile equally from both the front and back sides of the disc. This contrasts with the optically thick case, where a redshifted excess is induced in the lines around the planet due to the dominant front-side contribution (Figure 9). Line broadening associated with localized features in the disc-instability simulations remains symmetric in both optically thin and thick emission. Figure 24 shows the locations of peak velocity gradients in the azimuthal direction for the disc of HD 135344B, which help identify Doppler flips potentially associated with embedded planets (see Section 4.1.1). Finally, Figure 25 summarizes the extraction of large-scale kinematic structures in the disc of MWC 758, together with their pitch-angle and width profiles.

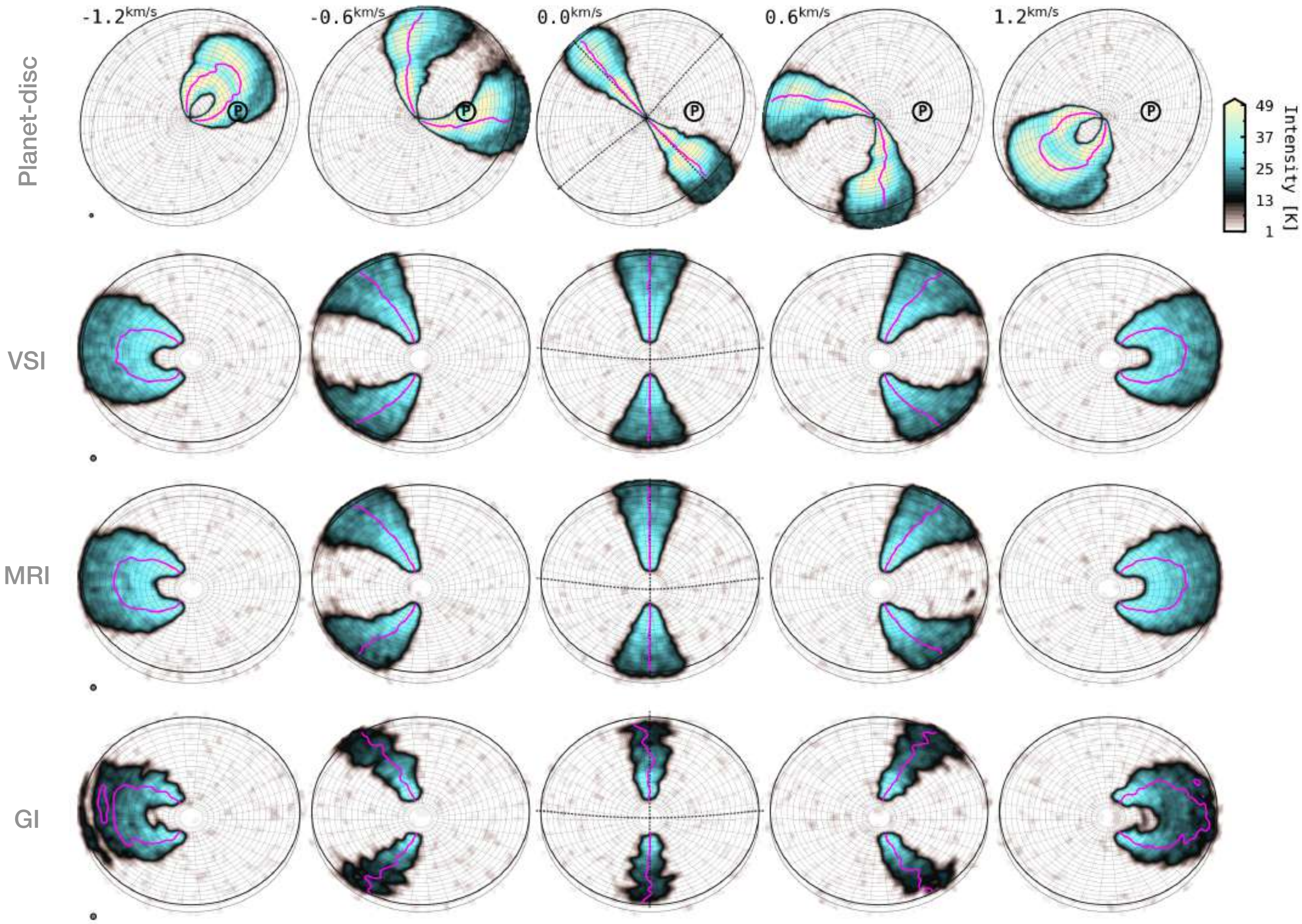

Figure 18. Selected ^{12}CO $J = 3$ 2 channel maps for the physical mechanisms studied in Section 3, shown for a disk inclination of $i = -30$. The channels in the top row correspond to synthetic observations of the planet–disk interaction model with a planet-to-star mass ratio of $q = 2 \times 10^{-3}$ and a planet azimuth of $\phi_p = -45$ in the disk reference frame; the projected planet location is labeled "P". The beam size is shown by the filled circle in the lower left of the first-column panels. The magenta line denotes the isovelocity contour at the velocity of each channel, measured from the corresponding centroid velocity map.

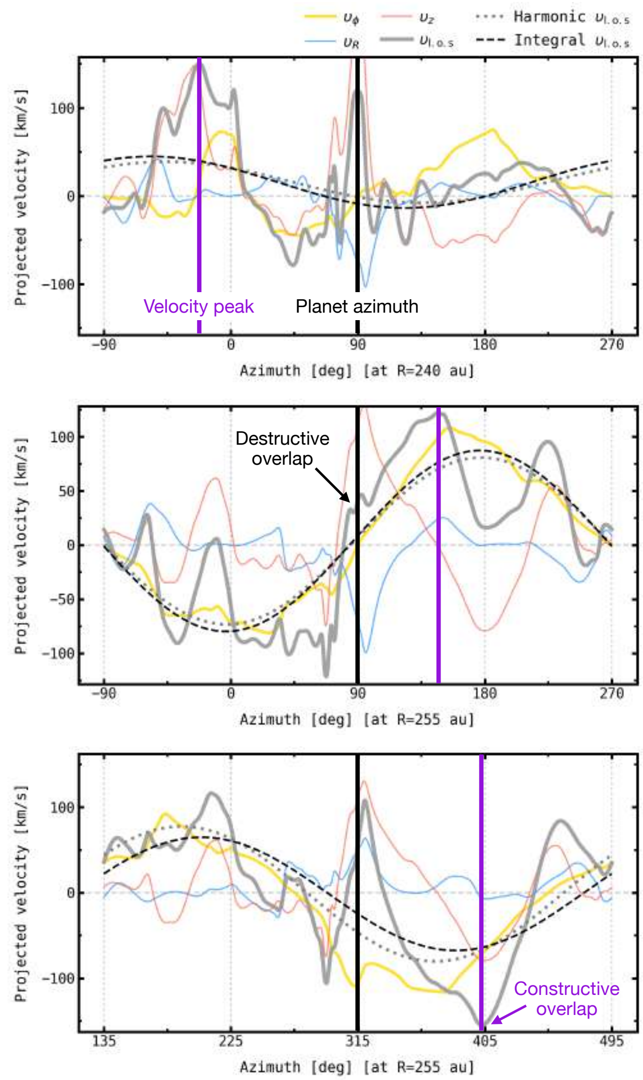

Figure 19. Illustrating how the combined contributions of velocity components from a planet–disk interaction simulation ($q = 2 \times 10^{-3}$, before postprocessing), after subtraction of Keplerian motion, can naturally produce peak line-of-sight velocity residuals at azimuthal locations far from the embedded planet, either through constructive overlap of the projected velocities away from the planet or destructive addition near it. The violet and black vertical lines denote the azimuth of the projected peak velocity and the true planet azimuth, respectively. The top two panels show azimuthal profiles of the projected velocities at radii of 240 au (top) and 255 au (middle) for a planet located at an azimuth of $\phi_p = 90$ and orbital radius $R_p = 240$ au. The bottom row is analogous to the middle but for a planet at $\phi_p = 315$. All projected velocities were computed assuming a disk inclination of -30 and an emission surface at $z/r = 0.2$. *Harmonic*$v_{\rm los}$ refers to the reconstructed velocity profile obtained by forward fitting the velocity components in the $v_{\rm los}$ equation (i.e., Equation 3 of A. F. Izquierdo et al. 2025), assuming they are constant in azimuth, while *Integral* $v_{\rm los}$ follows the analytic solution introduced in A. F. Izquierdo et al. (2023).

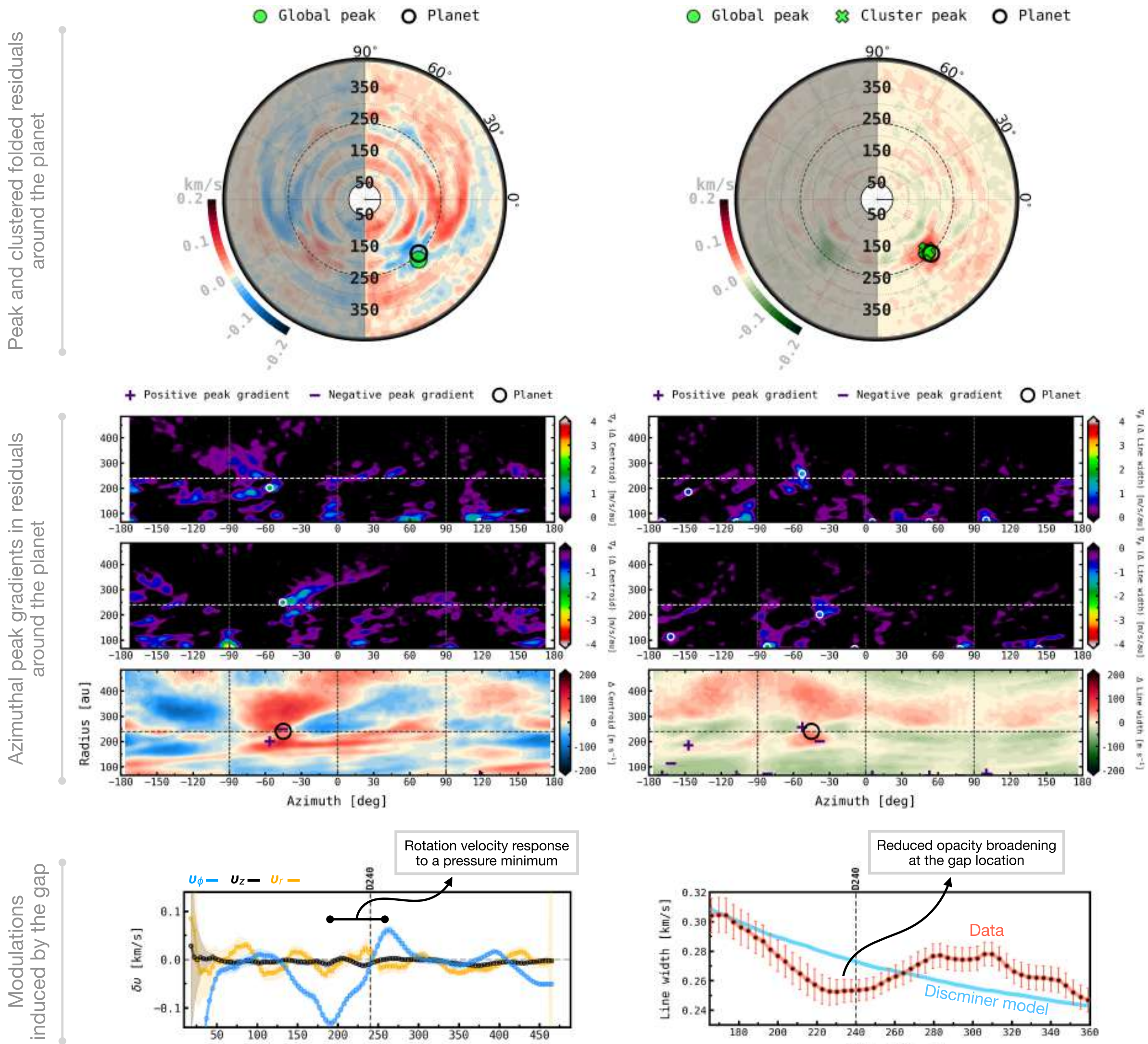

Figure 20. Summary of planet-driven signatures identified in the velocity and line-width residuals traced by [12]CO emission from a planet–disk interaction simulation with a planet-to-star mass ratio of $q = 2 \times 10^{-3}$, assuming a disc inclination of $i = -30°$ and post-processed with a fiducial beam size of 0\farcs15. The planet is embedded at an orbital radius of 240 au and an azimuth of −45 . See Section 3. for details on the simulation and postprocessing setups.

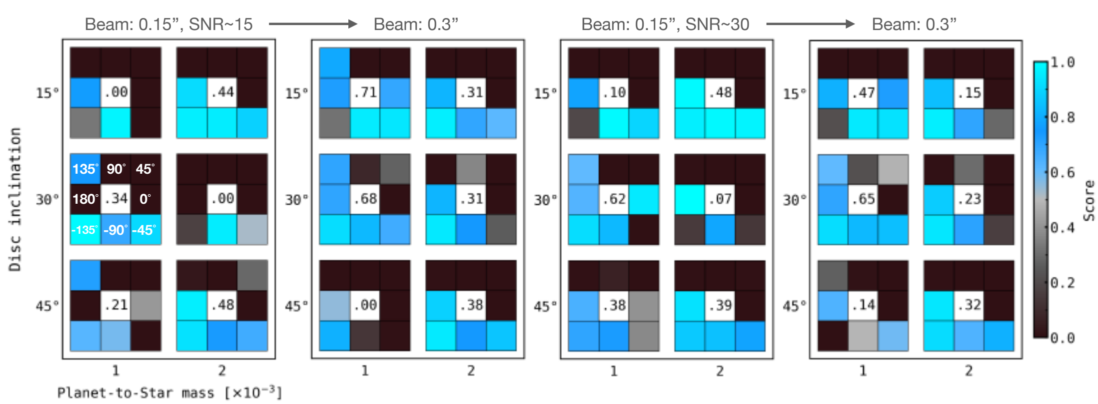

Figure 21. As Figure 5, but for detections based on localized velocity residuals.

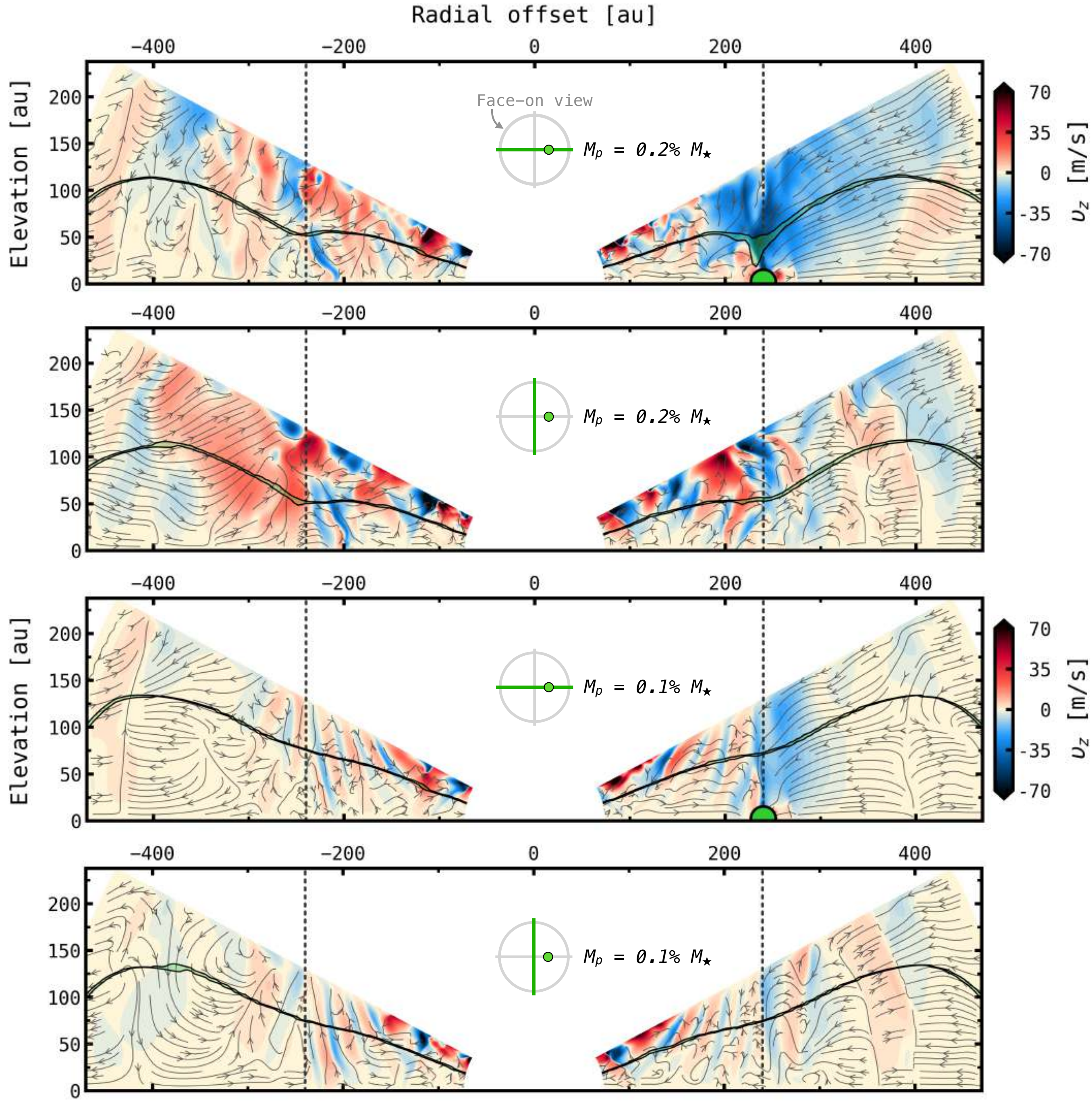

Figure 22. Edge-on slices of the vertical velocity component from the planet–disk interaction simulations presented in this work, overlaid with streamlines that incorporate the radial velocity field. The first and third panels from top to bottom show slices taken along the planet's azimuth, while the second and fourth panels depict slices perpendicular to it. Optical depth $\tau = 1$ surfaces representative of the ^{12}CO emitting region are overlaid as solid black curves, with the region between the minimum and maximum $\tau = 1$ elevations within a 10 wedge shaded in green. The strong localized downward flows around the planets are the primary drivers of the line-width enhancements and asymmetries identified in Section 3.

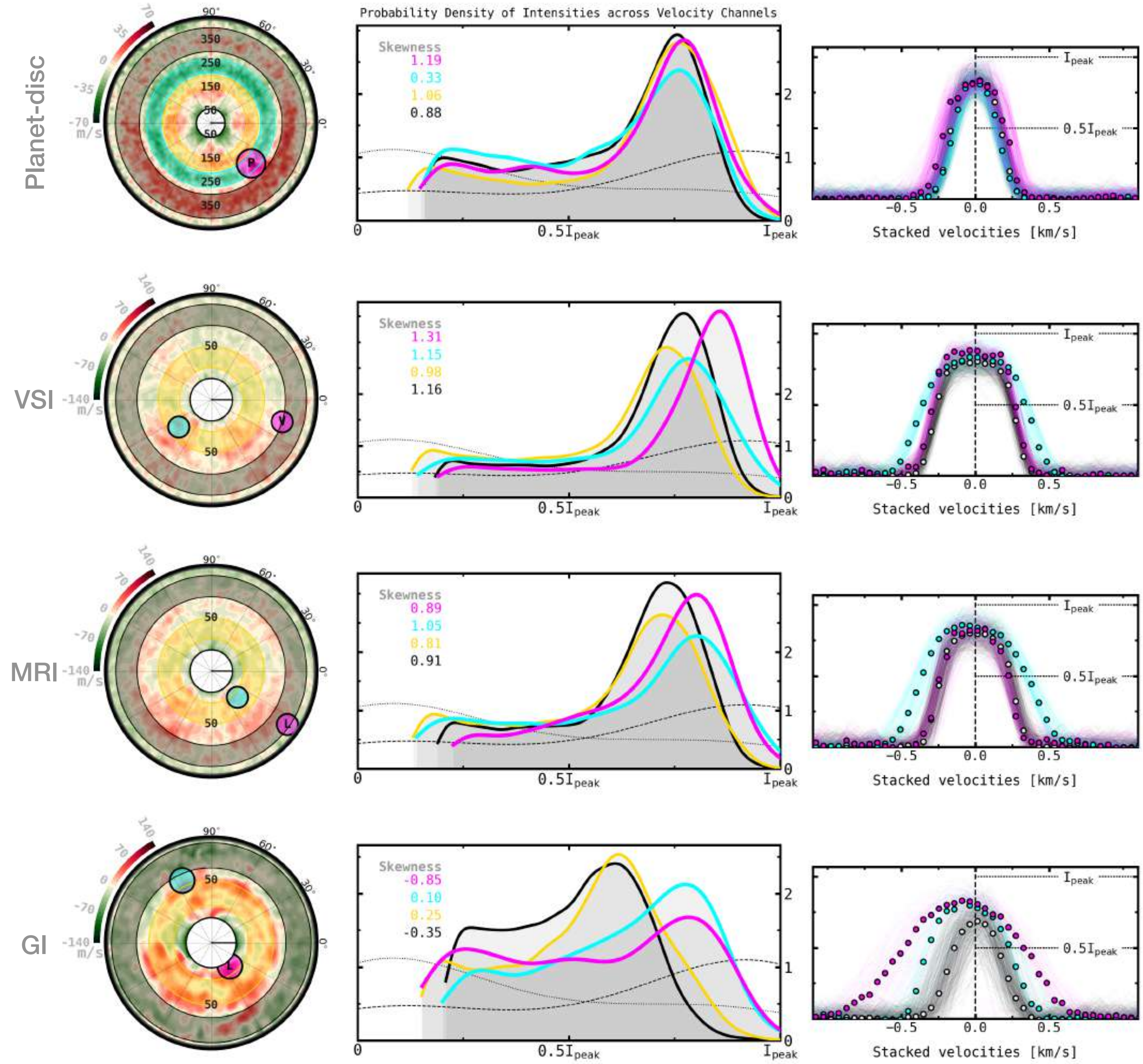

Figure 23. As Figure 9 but for synthetic cubes of ^{13}CO $J = 3$ 2 line emission, assuming a ^{12}CO/^{13}CO abundance ratio of 77.

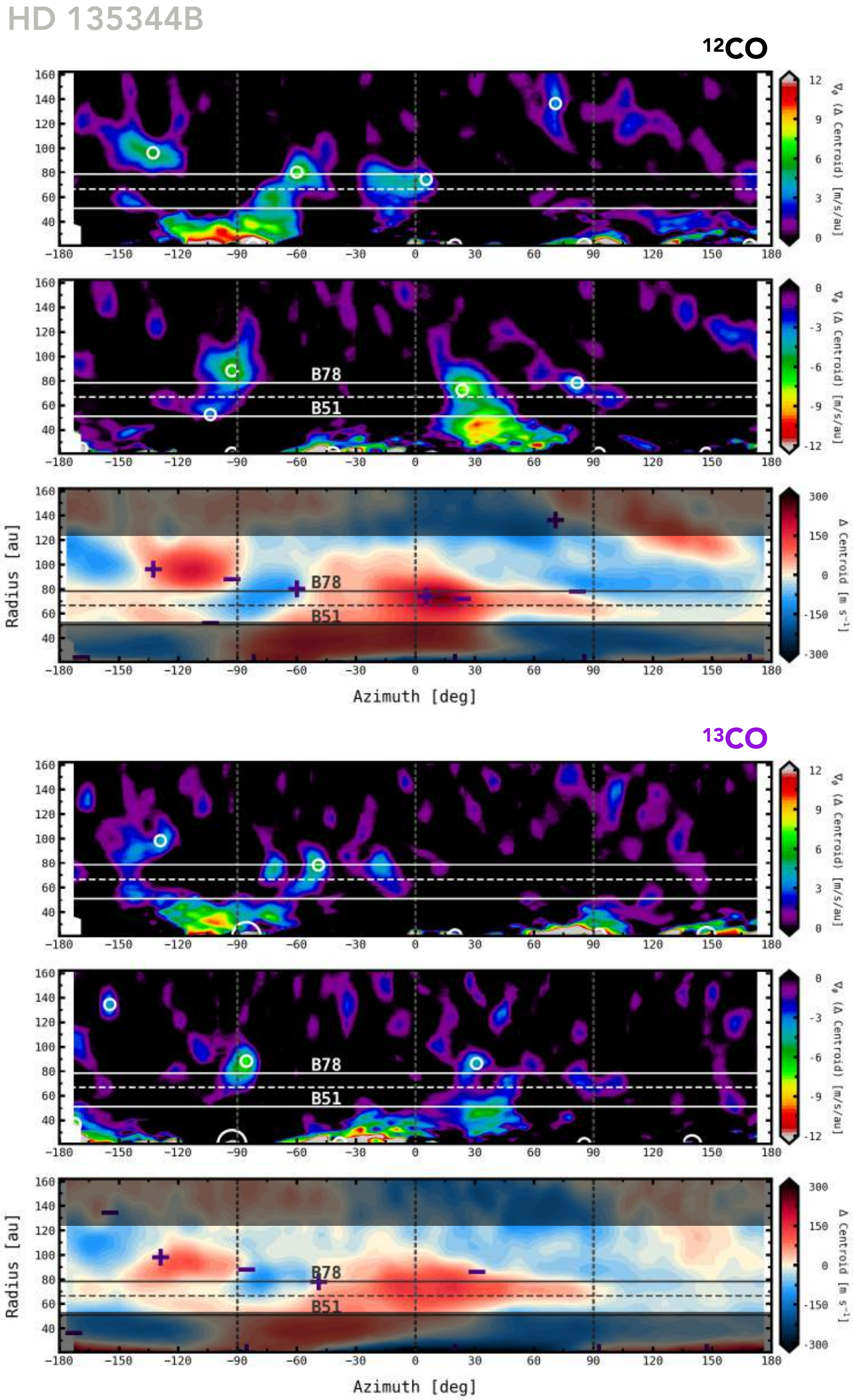

Figure 24. Polar maps illustrating the azimuthal gradients of the velocity residuals in the disk of HD 135344B, derived from ^{12}CO and ^{13}CO observations. The top and middle subpanels show the positive and negative gradient components, respectively, while the bottom panels display the corresponding velocity residuals, enabling the identification of Doppler-flip signatures in the kinematics. White circles mark the locations of the steepest gradients exceeding a threshold of 2.5 m s^{-1} au^{-1}, corresponding to velocity shifts greater than half the channel spacing per beam size (i.e., 50 m s^{-1} beam^{-1}). Pluses and minuses overlaid on the velocity residuals indicate the sign of the peak azimuthal gradients and highlight the central locations of the Doppler flips. Solid and dashed lines denote the radial separations of millimeter dust rings and gaps, respectively.

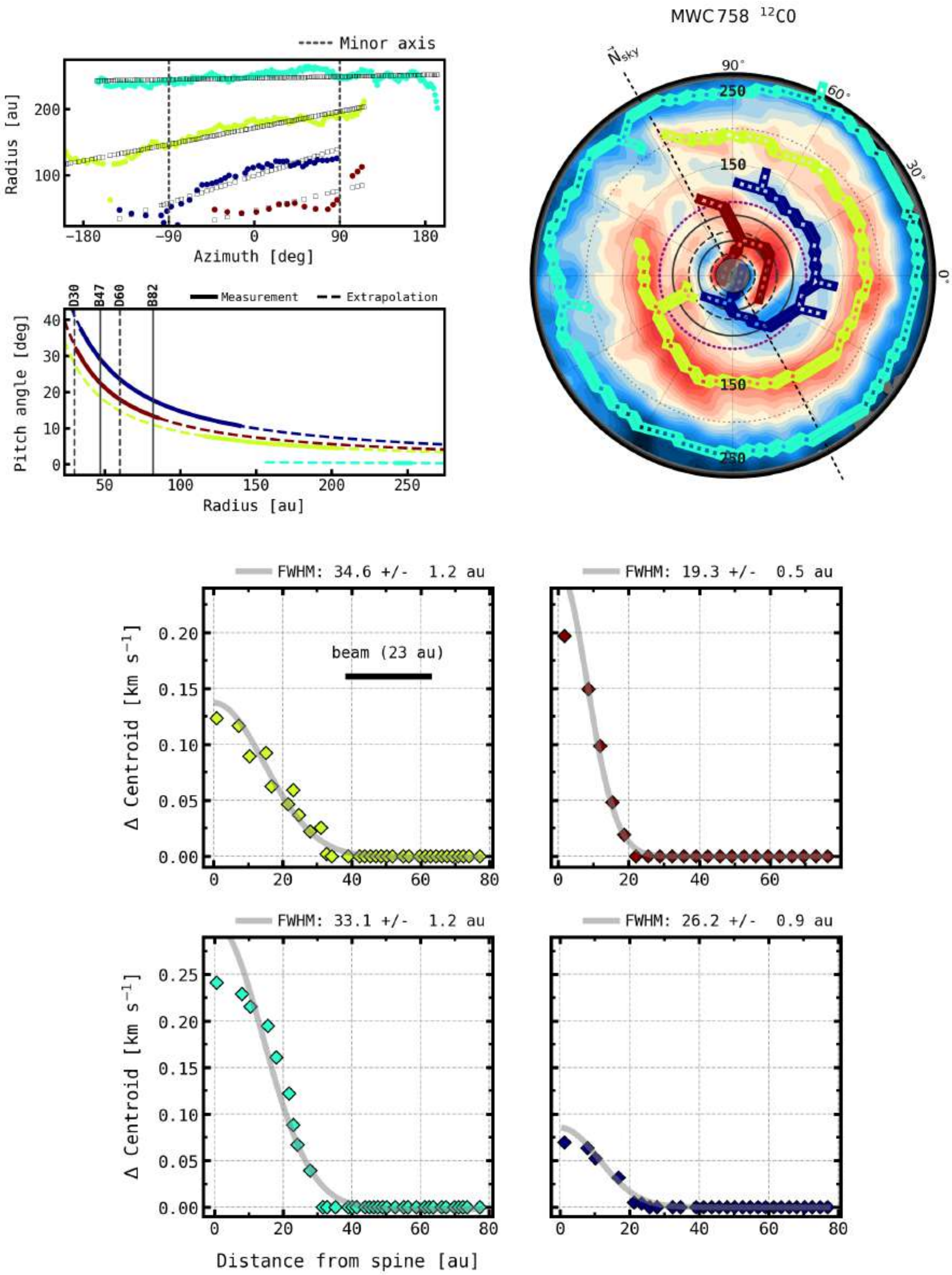

Figure 25. Extraction and characterization of coherent large-scale velocity substructures traced by ^{12}CO $J = 3$ 2 in the disk of MWC 758 using FILFINDER. The top panels illustrate the spatial configuration of the detected filaments, together with linear fits of the form $r = a + b\phi$ used to estimate the pitch angles of the observed substructures. The main nonaxisymmetric signature, traced in yellow across all panels, is well described by a tightly wound spiral with pitch angles <10 and dominated by downward vertical motions. The bottom panels display the average widths of the substructures, measured perpendicular to the medial axes of the filaments. Only the longest and outermost signatures (shown in yellow and cyan) are resolved by more than one resolution element.

ORCID iDs

Andrés F. Izquierdo https://orcid.org/0000-0001-8446-3026
Jaehan Bae https://orcid.org/0000-0001-7258-770X
Stefano Facchini https://orcid.org/0000-0003-4689-2684
Ewine F. van Dishoeck https://orcid.org/0000-0001-7591-1907
Marcelo Barraza-Alfaro https://orcid.org/0000-0001-6378-7873
Myriam Benisty https://orcid.org/0000-0002-7695-7605
Richard Teague https://orcid.org/0000-0003-1534-5186
Jochen Stadler https://orcid.org/0000-0002-0491-143X
Sean M. Andrews https://orcid.org/0000-0003-2253-2270
Gianni Cataldi https://orcid.org/0000-0002-2700-9676
Nicolás Cuello https://orcid.org/0000-0003-3713-8073
Pietro Curone https://orcid.org/0000-0003-2045-2154
Ian Czekala https://orcid.org/0000-0002-1483-8811
Daniele Fasano https://orcid.org/0000-0003-4679-4072
Mario Flock https://orcid.org/0000-0002-9298-3029
Misato Fukagawa https://orcid.org/0000-0003-1117-9213
Maria Galloway-Sprietsma https://orcid.org/0000-0002-5503-5476
Cassandra Hall https://orcid.org/0000-0002-8138-0425
Jane Huang https://orcid.org/0000-0001-6947-6072
John D. Ilee https://orcid.org/0000-0003-1008-1142
Andrea Isella https://orcid.org/0000-0001-8061-2207
Jensen Lawrence https://orcid.org/0009-0007-5371-3548
Geoffroy Lesur https://orcid.org/0000-0002-8896-9435
Giuseppe Lodato https://orcid.org/0000-0002-2357-7692
Cristiano Longarini https://orcid.org/0000-0003-4663-0318
Ryan A. Loomis https://orcid.org/0000-0002-8932-1219
François Ménard https://orcid.org/0000-0002-1637-7393
Christophe Pinte https://orcid.org/0000-0001-5907-5179
Daniel J. Price https://orcid.org/0000-0002-4716-4235
Giovanni Rosotti https://orcid.org/0000-0003-4853-5736
Leonardo Testi https://orcid.org/0000-0003-1859-3070
David J. Wilner https://orcid.org/0000-0003-1526-7587
Andrew J. Winter https://orcid.org/0000-0002-7501-9801
Lisa Wölfer https://orcid.org/0000-0002-7212-2416
Brianna Zawadzki https://orcid.org/0000-0001-9319-1296

References

Andrews, S. M., Huang, J., Pérez, L. M., et al. 2018, ApJL, 869, L41
Astropy Collaboration, Price-Whelan, A. M., Lim, P. L., et al. 2022, ApJ, 935, 167
Bae, J., Teague, R., Andrews, S. M., et al. 2022, ApJ, 934, L20
Bae, J., Flock, M., Izquierdo, A., et al. 2025, ApJL, 984, L12
Bae, J., Isella, A., Zhu, Z., et al. 2023, ASPC, 534, 423
Bae, J., Teague, R., & Zhu, Z. 2021, ApJ, 912, 56
Bae, J., Zhu, Z., & Hartmann, L. 2016, ApJ, 819, 134
Barraza-Alfaro, M., Flock, M., Béthune, W., et al. 2025, ApJL, 984, L21
Barraza-Alfaro, M., Flock, M., Marino, S., & Pérez, S. 2021, A&A, 653, A113
Baruteau, C., Barraza, M., Pérez, S., et al. 2019, MNRAS, 486, 304
Benisty, M., Izquierdo, A., & Stadler, J. 2026, ApJL, 1000, L14
Benisty, M., Juhasz, A., Boccaletti, A., et al. 2015, A&A, 578, L6
Benítez-Llambay, P., & Masset, F. S. 2016, ApJS, 223, 11
Béthune, W., & Latter, H. 2022, A&A, 663, A138
Blum, H. 1967, in Models for the Perception of Speech and Visual Form, ed. W. Wathen-Dunn (MIT Press), 362
Boehler, Y., Ricci, L., Weaver, E., et al. 2018, ApJ, 853, 162
Calcino, J., Christiaens, V., Price, D. J., et al. 2020, MNRAS, 498, 639
Calcino, J., Hilder, T., Price, D. J., et al. 2022, ApJL, 929, L25
CASA, T., Bean, B., Bhatnagar, S., et al. 2022, PASP, 134, 114501
Casassus, S., Christiaens, V., Cárcamo, M., et al. 2021, MNRAS, 507, 3789
Casassus, S., & Pérez, S. 2019, ApJL, 883, L41
Cazzoletti, P., van Dishoeck, E. F., Pinilla, P., et al. 2018, A&A, 619, A161
Cugno, G., Leisenring, J., Wagner, K. R., et al. 2024, AJ, 167, 182
Curone, P., Facchini, S., Andrews, S. M., et al. 2025, ApJL, 984, L9
Dartois, E., Dutrey, A., & Guilloteau, S. 2003, A&A, 399, 773
Dong, R., Liu, S.-y., Eisner, J., et al. 2018, ApJ, 860, 124
Dong, R., Liu, S.-Y., & Fung, J. 2019, ApJ, 870, 72
Dong, R., Zhu, Z., Rafikov, R. R., & Stone, J. M. 2015, ApJL, 809, L5
Dullemond, C. P., Juhasz, A., Pohl, A., et al. 2012, RADMC-3D: A multi-purpose radiative transfer tool, Astrophysics Source Code Library, 1202.015
Fairlamb, J. R., Oudmaijer, R. D., Mendigutía, I., Ilee, J. D., & van den Ancker, M. E. 2015, MNRAS, 453, 976
Flock, M., Ruge, J. P., Dzyurkevich, N., et al. 2015, A&A, 574, A68
Flock, M., Turner, N. J., Nelson, R. P., et al. 2020, ApJ, 897, 155
Foreman-Mackey, D., Hogg, D. W., Lang, D., & Goodman, J. 2013, PASP, 125, 306
Fukagawa, M., Izquierdo, A., & Facchni, S. 2026, ApJL, 1000, L15
Gaia Collaboration, Vallenari, A., Brown, A. G. A., et al. 2023, A&A, 674, A1
Galloway-Sprietsma, M., Bae, J., Izquierdo, A. F., et al. 2025, ApJL, 984, L10
Garufi, A., Quanz, S. P., Avenhaus, H., et al. 2013, A&A, 560, A105
Ginsburg, A., Koch, E., Robitaille, T., et al. 2019, radio-astro-tools/spectral-cube: Release v0.4.5, Zenodo, doi: 10.5281/zenodo.3558614
Grady, C. A., Muto, T., Hashimoto, J., et al. 2013, ApJ, 762, 48
Hacar, A., Alves, J., Burkert, A., & Goldsmith, P. 2016, A&A, 591, A104
Hall, C., Dong, R., Teague, R., et al. 2020, ApJ, 904, 148
Harris, C. R., Millman, K. J., van der Walt, S. J., et al. 2020, Natur, 585, 357
Hunter, J. D. 2007, CSE, 9, 90
Izquierdo, A. F., Bae, J., Galloway-Sprietsma, M., et al. 2026, ApJL, 997, L2
Izquierdo, A. F., Facchini, S., Rosotti, G. P., van Dishoeck, E. F., & Testi, L. 2022, ApJ, 928, 2
Izquierdo, A. F., Stadler, J., Galloway-Sprietsma, M., et al. 2025, ApJL, 984, L8
Izquierdo, A. F., Testi, L., Facchini, S., Rosotti, G. P., & van Dishoeck, E. F. 2021, A&A, 650, A179
Izquierdo, A. F., Testi, L., Facchini, S., et al. 2023, A&A, 674, A113
Koch, E., Ginsburg, A., AKL, et al. 2021, radio-astro-tools/radio-beam: v0.3.3, Zenodo, doi: 10.5281/zenodo.4623788
Koch, E. W., & Rosolowsky, E. W. 2015, MNRAS, 452, 3435
Law, C. J., Booth, A. S., & Öberg, K. I. 2023, ApJL, 952, L19
Lesur, G., Flock, M., Ercolano, B., et al. 2023, ASPC, 534, 465
Leys, C., Ley, C., Klein, O., Bernard, P., & Licata, L. 2013, JESP, 49, 764
Longarini, C., Lodato, G., Rosotti, G., et al. 2025, ApJL, 984, L17
Loomis, R. A., Facchini, S., Benisty, M., et al. 2025, ApJL, 984, L7
Maio, F., Fedele, D., Roccatagliata, V., et al. 2025, A&A, 699, L10
Mao, S., Dong, R., Lu, L., et al. 2023, ApJL, 950, L12
Mignone, A., Bodo, G., Massaglia, S., et al. 2007, ApJS, 170, 228
Miotello, A., Kamp, I., Birnstiel, T., Cleeves, L. C., & Kataoka, A. 2023, ASPC, 534, 501
Muto, T., Grady, C. A., Hashimoto, J., et al. 2012, ApJL, 748, L22
Öberg, K. I., Facchini, S., & Anderson, D. E. 2023, ARA&A, 61, 287
Öberg, K. I., Guzmán, V. V., Walsh, C., et al. 2021, ApJS, 257, 29
Pérez, S., Casassus, S., & Benítez-Llambay, P. 2018, MNRAS, 480, L12
Pinte, C., Price, D. J., Ménard, F., et al. 2018, ApJL, 860, L13
Pinte, C., Teague, R., Flaherty, K., et al. 2023, ASPC, 534, 645
Pinte, C., van der Plas, G., Ménard, F., et al. 2019, NatAs, 3, 1109
Pinte, C., Ilee, J. D., Huang, J., et al. 2025, ApJL, 984, L15
Rabago, I., & Zhu, Z. 2021, MNRAS, 502, 5325
Ragusa, E., Lynch, E., Laibe, G., Longarini, C., & Ceppi, S. 2024, A&A, 686, A264
Reggiani, M., Christiaens, V., Absil, O., et al. 2018, A&A, 611, A74
Ren, B., Dong, R., van Holstein, R. G., et al. 2020, ApJL, 898, L38
Ren, B. B., Benisty, M., Ginski, C., et al. 2023, A&A, 680, A114
Rosotti, G. P., Teague, R., Dullemond, C., Booth, R. A., & Clarke, C. J. 2020, MNRAS, 495, 173
Schwarz, K. R., Bergin, E. A., Cleeves, L. I., et al. 2016, ApJ, 823, 91
Speedie, J., Dong, R., Hall, C., et al. 2024, Natur, 633, 58
Stadler, J., Benisty, M., Izquierdo, A., et al. 2023, A&A, 670, L1
Stadler, J., Benisty, M., Winter, A. J., et al. 2025, ApJL, 984, L11
Stolker, T., Dominik, C., Avenhaus, H., et al. 2016, A&A, 595, A113
Teague, R., Bae, J., Aikawa, Y., et al. 2021, ApJS, 257, 18
Teague, R., Bae, J., Bergin, E. A., Birnstiel, T., & Foreman-Mackey, D. 2018, ApJL, 860, L12
Teague, R., Bae, J., & Bergin, E. A. 2019, Natur, 574, 378
Teague, R., Benisty, M., Facchini, S., et al. 2025, ApJL, 984, L6
Teague, R., & Foreman-Mackey, D. 2018, RNAAS, 2, 173

van der Marel, N., Cazzoletti, P., Pinilla, P., & Garufi, A. 2016, ApJ, 832, 178
van der Velden, E. 2020, JOSS, 5, 2004
van der Walt, S., Schönberger, J. L., Nunez-Iglesias, J., et al. 2014, PeerJ, 2, e453
Virtanen, P., Gommers, R., Burovski, E., et al. 2020, scipy/scipy: SciPy 1.5.3, Zenodo, doi:10.5281/zenodo.4100507
Visser, R., van Dishoeck, E. F., & Black, J. H. 2009, A&A, 503, 323
Wagner, K., Stone, J., Skemer, A., et al. 2023, NatAs, 7, 1208
Winter, A. J., Benisty, M., Izquierdo, A. F., et al. 2025, ApJL, 990, L10
Wölfer, L., Barraza-Alfaro, M., Teague, R., et al. 2025, ApJL, 984, L22
Wölfer, L., Facchini, S., van der Marel, N., et al. 2023, A&A, 670, A154
Xie, C., Xie, C., Ren, B. B., et al. 2024, Univ, 10, 465